

Contents

1	Belle II and SuperKEKB (SKB) accelerator	4
1.1	Physics program of the B-factories	4
1.1.1	Opened questions in SM	4
1.1.2	Belle II Physics channels	5
1.1.3	B meson decay vertices	7
1.2	SuperKEKB accelerator	8
1.2.1	The facility	8
1.2.2	"Nano-beam" scheme	10
1.3	Belle II detector	11
1.3.1	Vertex Detector (VXD)	11
1.3.2	Central Drift Chamber (CDC)	12
1.3.3	Particle identification system (TOP e ARICH)	12
1.3.4	Electromagnetic calorimeter (ECL)	13
1.3.5	K_L muon detector (KLM)	13
1.3.6	Trigger system	14
1.4	Current state and perspectives of data taking	14
2	TJ-Monopix 2	15
2.1	Matrix and flavors	15
2.1.1	Flavors	16
2.1.2	Pixel design	17
2.1.2.1	Improved front-end circuit design	18

2.2	Threshold and noise	19
2.2.1	S-Curve method	19
2.2.1.1	Normal FE	20
2.2.1.2	Cascode FE	20
2.2.1.3	HV-Cascode FE	21
2.2.1.4	HV-Normal FE	23
2.2.1.5	Summary Table	24
2.2.2	Threshold dispersion and tuning	26
2.2.2.1	Results from fine tuning	27
2.3	ToT calibration with internal injection	27
2.3.1	Injection circuit issues	27
2.3.2	Time Over Threshold (TOT) curves and fit	28
2.4	Response to radioactive source and absolute calibration	29
2.4.1	^{55}Fe	30
2.4.2	^{241}Am	30
2.4.3	^{109}Cd	32
2.4.4	Injection capacitance calibration	32
2.4.5	Check on linearity of tot fit	35
2.5	Operation with low threshold	35
2.5.1	Register optimization	37
2.5.2	Comparison between data and simulation	38
2.5.2.1	I_{CASN}	38
2.5.2.2	I_{THR}	39
2.5.2.3	Time over Threshold (ToT)	40
2.5.2.4	some nice picture of the optimized thr and tuning	40
2.6	Cross talk issue and mitigation	40
2.6.1	Hot pixel issue	41
2.6.2	Hot pixel strategy (study)	43
2.6.3	Cross-talk (Results)	45
2.6.4	Mitigation	47

2.6.4.1	Final results?	50
2.7	Test Beam results	50
3	Conclusions	51

1. Belle II and SuperKEKB (SKB) accelerator

This first chapter aims to present a brief introduction of the Belle II physics program, focusing on those measurements which could particularly benefit from the upgrade of the whole detector and in particular of the VerteX Detector (VXD), discussed in this work. A short description of the SuperKEKB accelerator's operation, the Belle II detector's structure and to conclude some highlights on the actual state of measurements are also presented.

1.1 Physics program of the B-factories

Belle II is a B-factory dedicated to improve precision measurements of the Standard Model's parameters (SM) and to looking for the physics Beyond the Standard Model (BSM). In particular the experiment investigates the Charge-Parity Violation (CPV) in the B mesons system and it also searches for New Physics (NP) evidences in the decays of B and D mesons, in τ leptons and in the dark matter sector (DM), above all, hunting for dark photons.

1.1.1 Opened questions in SM

The SM is a physics theory that describes three of the fundamental forces [interactions] involving elementary particles, which are strong, weak and electromagnetic interaction (with the exclusion of the gravitational one). It classifies all known particles up to now in 4 main groups: quarks, leptons, bosons and Higgs (figure 1.1 on the facing page).

Despite its undeniable success achieved over the years in predicting with high precision new particles and mechanisms unknown until that moment, there are many aspects of the Nature on which it is unable to give answers. Some of them are listed in the following.

- Three generations of quark and leptons are known, but it is not obvious whether they should be the only ones and the reasons behind their mass hierarchy.
- Higgs mechanism is able to explain the cause of elementary particles' masses through spontaneous electro-weak symmetry breaking, but it doesn't justify those of neutrinos.



Figure 1.1: Particle classification in the Standard Model.

- The SM also predicts other Higgs-like bosons, potentially vector bosons, whose existence would be justified in some SUper-SYmmetry (SUSY) theories or in others of New Physics.
- Another opened question is the matter-antimatter asymmetry in the Universe. Even though CP violation is necessary to explain the current state of the universe, the observed quantity is several orders of magnitude less than needed to explain the matter domination over antimatter, which allowed the evolution of the universe as we know it today.
- The elements of the Cabibbo-Kobayashi-Maskawa (CKM) matrix, which complex phase is at the foundation of CP Violation (CPV) in the quark flavor sector, are diagonal and it might suggest the existence of a new symmetry, that is unbroken at high energy (greater than the order of TeV).

All these topics encourage the research of new particles and processes that could give reasonable answers.

At the energy frontier, experiments like the Large Hadron Collider (LHC) in Geneve are looking for new particles created from the proton-proton collision with a center mass energy up to 14 TeV.

At luminosity frontier instead, the trace of new particles and mechanisms is searched in precision measurements of suppressed reactions in flavour physics or in the deviations from SM. The discrepancies indeed, could be interpreted as a clue of new physics beyond SM. The last is the Belle II approach.

1.1.2 Belle II Physics channels

The field of reaserch at SuperKEKB is very extended and in the following we will go through the main physics goals of the experiment, underlining how the

measurements could be enhanced by the upgrade of the vertex detector.

FLAVOR PHYSICS

CP-violating phases in quark sector:

- as we mentioned above, the amount of CP violation in the SM is not enough to explain the difference observed between baryon-antibaryon matter. New clues of CPV could be found studying the discrepancy between B^0 and \bar{B}_0 decay rates, so measuring the time-dependent CP violation in penguin transition of $b \rightarrow s$ and $b \rightarrow d$ quarks (such as $B \rightarrow \phi K^0$ and $B \rightarrow \eta' K^0$). In fact this violation is expected to be very small in the SM, so any significant observation of CPV can be interpreted as a signal beyond the SM.
- Also the CP violation in charm mixing, negligible in the SM, could draw attention to new phenomena in the up-type quark sector.
- Another aspect that need to be understood is the large amount of CP violation in the time-integrated rates of charmless hadronic B decays, such as $B \rightarrow K\pi$ and $B \rightarrow K\pi\pi$, observed by other B factories and LHCb.

Conclusive measurements of time-dependent CP violation require a combination of data size and high precision measurement of Δz (discussed further in on the next page), the distance between the tag and signal in B meson decay vertices. In this respect, the upgrade of VXD could improve a lot the flavor tagging efficiency losses, due mainly to the beam-induced backgrounds, among the others.

Multiple Higgs bosons: Another fundamental channel is the measurement of the Branching Ratio (BR) of $B \rightarrow \tau\nu$, which is particularly sensitive to the charged Higgs boson (in addition to a neutral SM-like Higgs) that in general couples more strongly to heavier particles. But also the BR of the decay $B \rightarrow D^{(*)}\tau\nu$, where BaBar, Belle and LHCb had already reported some anomalies. Moreover extended Higgs mechanism could introduce extra sources of CP violation. We could notice that semi-tauonic decay measurements, rely on efficient and pure tag side B full reconstruction, and so also on the performance of VXD.

Flavor Changing Neutral Current (FCNC):

- For this purpose, measurements of time-dependent CP violation in $B \rightarrow K^{*0}(\rightarrow K_S^0 \pi^0)\gamma$, triple product CP violation asymmetries in $B \rightarrow VV$ decays, and semileptonic decays $B \rightarrow Vl\nu$, $V = D^*$, ρ are the main approaches.
- It is also important to measure $b \rightarrow s\nu\bar{\nu}$ transitions (such as $B \rightarrow K^{(*)}\nu\bar{\nu}$) which belong to a class of decays with large missing energy and to improve FCNC measurements of $b \rightarrow d$, $b \rightarrow s$, and $c \rightarrow u$ transitions.

Most analyses with missing energy in the final state utilise hadronic or semileptonic B full reconstruction techniques and the performance of these methods is most dependent on low momentum track finding and so on the capabilities of the vertex detector as well.

Sources of Lepton Flavor Violation (LFV): LFV in charged lepton decay (at rates of 10^{-8}) is a key prediction in many neutrinos mass generation mechanisms and other models of physics BSM. Belle II has an unrivalled sensitivity to τ decays, because of their production in a clean e^+e^- collision background and the large dataset. The experiment analyzes τ leptons to search for LF and CP violation and to measure its the electric dipole moment and (g-2) value.

NON FLAVOR PHYSICS

Dark Sector: Belle II has a unique sensitivity to dark matter via missing energy decays. Although most research for NP are indirect, there are different model that predict the existance of new particles at the MeV to GeV scale, that couple to the SM via new gauge asymmetries. They also predict a vast range of hidden particles, including dark matter candidates and new gauge bosons.

In these last two areas, τ and dark sectors physics, the aim is to probe forbidden and ultra-rare transition in low-multiplicity final states with as large dataset as possible. This mostly relies on trigger efficiency and strategies, that could take advantage from the upgrade. Many of these processes can only be addressed by Belle II, so it is essential to increase the perfomance of the detector.

Binding Hadrons: As time goes on, a large numbers of states not predicted by conventional mesons interpretation are discovered in other B factories and hadron colliders, changing our understanding of QCD in the low-energy regime. For this reason, study of quarkonia is a fundamental purpose for Belle II. In fact new particles can be produced near resonance, achievable by adjusting the machine energy, or by intial state radiation, which effectively provides a continuum of center of mass energies.

CKM matrix: Belle II is also dealing with the measurements of CKM observable, the matrix elements and their phases, with unprecedented precision.

1.1.3 B meson decay vertices

In the topology of the B meson decay vertices, lie the combined great efforts employed to be able to build a fast, high-granularity and radiation hardness detector. As a matter of fact the main task of VXD is the reconstruction of the production and decay vertices of the particle produced in the collision. It is crucial to perform time-dependent measurements, core of the Belle II physics program.

The center of mass energy of Belle II experiment has its peak at the $\Upsilon(4S)$ resonance, such as $\sqrt{s} = 10.58$ GeV, which decays into two B mesons ($B^0 \bar{B}^0$)

in nearly 100% of all cases. The choice of the asymmetric configuration of the beams, relies precisely in the requirement to boost the mesons in order to measure their life-time, exploiting the information on the distance between their decay vertices. More precisely, the investigation of CP Violating processes requires to measure the decay time difference of the two B mesons, and its uncertainty is dominated by that of decay vertex measurement (order of hundreds microns).

The six-layer VXD allows to determine the position of the vertices with a precision better than 100 μm , allowing to reconstruct secondary vertices, i.e. the decay position of the particles coming from B decays, and also the tau and D mesons vertices, widening the Belle II physics program to charm and tau physics. ??

1.2 SuperKEKB accelerator

Belle II sensitivity in the precision measurements that we sift through in the previous section, is feasible especially thanks to the extraordinary performance of the SuperKEKB accelerator which host the (almost) hermetic detector. This complex facility is the result of efforts and efficient collaboration between the researches of KEK laboratory and all the international working groups that participate to the experiment.

1.2.1 The facility

SuperKEKB is an asymmetric e^+e^- collider with a circumference of 3 km and a center of mass energy peak equal to $\sqrt{s} = 10.58 \text{ GeV}$, which corresponds to the mass of the $\Upsilon(4S)$ resonance. Compared to its predecessor KEKB (which started its operation in 1998 and concluded in 2010), the current accelerator has allowed to obtain the highest luminosity ever achieved, equal to $4.7 \times 10^{-34} \text{ cm}^{-2}\text{s}^{-1}$ in July 2022, using a new scheme to accelerate and collide the beams, the so called *nano-beam scheme*(section 1.2.2 on page 10). Moreover a new upgrade of the machine, still under study, will also include other interventions especially to cope with higher background levels, in view of further increase in luminosity.

We will briefly see the main features and parameters of the accelerator.

Luminosity

Luminosity is one of the key parameters of an accelerator and it represents the interaction rate per unit of cross section between colliding particles. Reversing this equation is possible to obtain N, namely the number of the physical events produced in the interaction with a given luminosity:

$$L = \frac{1}{\sigma} \frac{dN}{dt} \quad \Rightarrow \quad N = \int_0^T L \sigma dt \quad (1.1)$$

where T is the duration of the experiment, σ the cross section of the physical process of interest. Specifically luminosity is strictly dependent from both machine parameters and the main characteristics of the beam. With respect to this, it can be expressed as:

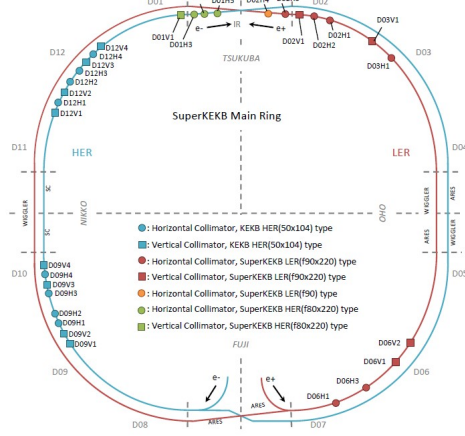


Figure 1.2: SuperKEKB accelerator in 2021. The letters V and H denote respectively vertical and horizontal collimators. Each ring is divided in 12 sections, from the first called D01 to the last D12.

$$L = \dots \quad (1.2)$$

where

As we have already seen, SuperKEKB holds the actual world record in luminosity (with $\beta_y^* = 1.0$ mm) and in the near future the target will be to reach $6.3 \times 10^{-35} \text{ cm}^{-2}\text{s}^{-1}$, by increasing current beams and reducing their section in the Interaction Point (IP), through the reduction of the betatron function to $\beta_y^* = 0.3$ mm.

For these reasons, the supervision of the beams background becomes crucial: right now it has been estimated that the background should remain acceptable up to a luminosity value equal to $2.8 \times 10^{-35} \text{ cm}^{-2}\text{s}^{-1}$ with $\beta_y^* = 0.6$ mm. So the possibility(hope) to achieve higher luminosity is closely (strictly) related to an upgrade plan of both the detector and the accelerator.

Beam energy

Energy beams is mostly decided by the physics program interesting for the experiment. Currently SuperKEKB collides an electron beam with energy of 7 GeV (High Energy Ring, HER), with a positron beam of 4 GeV (Low Energy Ring, LER), reaching a center of mass energy peaked to $\Upsilon(4S)$ resonance.

The choice of colliding asymmetric beam (like its predecessor KEKB, which got collide electrons beam of 8 GeV with a positrons beam of 3.5 GeV) is necessary to identify and measure the decay vertices of particles created in the collisions, as we have seen in section 1.1.3 on page 7.

Indeed this mechanism allows to boost the decay products, improving the vertices reconstruction and increasing the sensitivity of the physics measurement, too. In particular this makes possible time-dependet measurements, especially in CP violation.

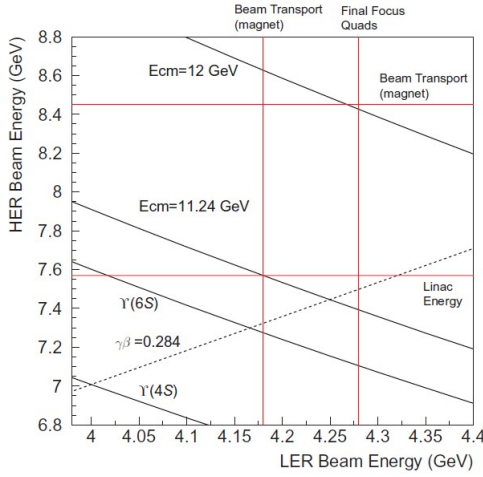


Figure 1.3: Beam energies to reach center of mass energy equal to $\Upsilon(4S)$, $\Upsilon(6S)$, 11.24 GeV and 12 GeV. Horizontal axis represents the energy of LER and the vertical one the energy of HER.

In figure 1.3 the flexibility of the energy of both LER and HER beams is showed, which provides a continuum of the center mass energy. The possible range covers energies which goes from the $\Upsilon(1S)$ (9.46 GeV) resonance to the $\Upsilon(6S)$ (11.24 GeV).

1.2.2 "Nano-beam" scheme

[?]

As mentioned in the previous section, another decisive factor to define the luminosity is the *beta function* β in the Interaction Point (IP). To be able to increase luminosity, it's necessary to decrease the value of β depending also but not only, on the variation of the other machine parameters in the definition (on the previous page). The mechanism used in SuperKEKB is called *nano-beam scheme*, and it allowed to obtain luminosity 40 times greater than that of KEKB, managing to (succeeding) decrease of 1/20 the β function in the IP.

This new scheme, designed by P. Raimondi, dictates that the beams have to collide at large angle, equal to 83 mrad in SuperKEKB (keeping beams divided through quadrupole magnets), in order to reduce the *hourglass effect*, which succeed when the bunches in the beam are much longer.

Using a crossing angle large enough, has other positive implications on the operation of the accelerator:

- allows the placement of a new focusing system in the IP with a superconducting quadrupole magnet;
- allows to have two distinct line which host HER and LER beams;
- diminishes the *fringe fields* effect in the IP, which are the residuals of the magnets (magnetic fields) in the proximity (nearby).

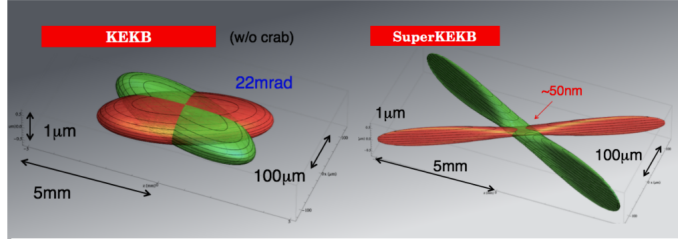


Figure 1.4: Comparison between the beams scheme used in KEKB and SuperKEKB.

1.3 Belle II detector

Belle II detector is a general-purpose spectrometers, which consists of a series of nested subdetectors that surrounds the IP of the two beams, placed around the berillium beam pipe of 10 mm of radius. Here we will go through a briefly description of the several subdetectors.

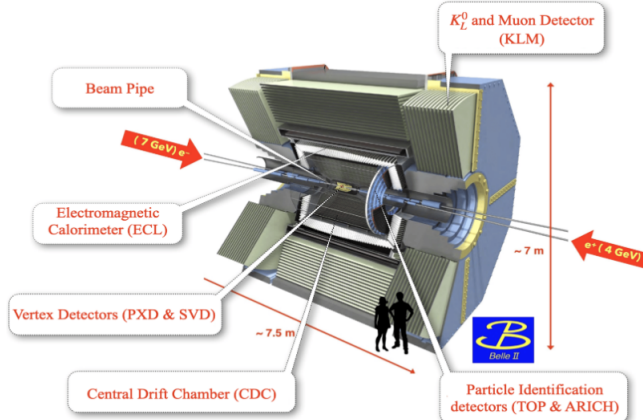


Figure 1.5: Belle II detector.

1.3.1 Vertex Detector (VXD)

The **VerteX Detector (VXD)** is composed by two devices, the silicon Pixel Detector (PXD) and the Silicon Vertex Detector (SVD), for a total of six layers around the beam pipe.

The inner two layers of PXD (L12) consist of pixelated sensors based on the depleted field effect transistor (DEPFET) technology, realised with very thin ($< 100 \mu\text{m}$) sensors, allowing to minimise multiple scattering, thus improving the tracking resolution for low-momentum particles. They are at a radius of 14 mm and 22 mm, respectively.

The remaining four layers of SVD (L3456) instead, are equipped with double-sided silicon strip (DSSD) sensors (at 39 mm, 80 mm, 104 mm and 135 mm respectively). Since a lower background rate is expected with respect to PXD,

DSSD allow to achieve similar performance with a much smaller number of readout channels. These layers are mainly used for tracking/vertexing and also for particle identification (dE/dx).

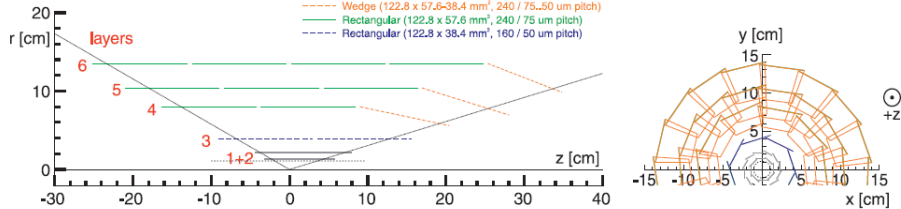


Figure 1.6: A schematic view of the Belle II vertex detector with a Be beam pipe and the six layers of PXD and SVD.

1.3.2 Central Drift Chamber (CDC)

It is the central tracking device, with a large-volume drift chamber and small drift cells. The chamber gas is composed of a $\text{He}-\text{C}_2\text{H}_6$ 50:50 mixture with an average drift velocity of $3.3 \mu\text{s}^{-1}$ and a maximum drift time of about 350 ns for a 17 mm cell size. The CDC contains 14336 wires arranged in 56 layers either in *axial* (so aligned with the solenoidal magnetic field) or *stereo* (skewed with respect to the axial wires) orientation. In fact by combining information from both the axial and the stereo layers it is possible to reconstruct a full three-dimensional helix charged tracks and measures their momenta. It also provides information for particle identification by measuring ionization energy loss, which is particularly useful for low-momentum particles that cannot reach the outer particle identification subdetectors.

1.3.3 Particle identification system (TOP e ARICH)

TOP (Time Of Propagation) is a special kind of Cherenkov detector used for particle identification in the barrel region. It employs the two-dimensional information of a Cherenkov ring image, such as the time of arrival and impact position of Cherenkov photons at the photodetector at one end of a 2.6 m quartz bar. It is composed by 16 detector modules, each one consisted in a 45 x 2 cm quartz bar (Cherenkov radiator) with a small expansion volume (about 10 cm long) at the sensor end of the bar. In order to achieve a single-photon time resolution of about 100 ps (required for a good PID), 16-channel microchannel plate photomultiplier tubes (MCP-PMT), specially developed for this purpose, are employed.

ARICH (Aerogel Ring Imaging CHerenkov) is used to identify charged particle and it is placed in the forward endcap region. It is a proximity focusing Cherenkov ring imagine detector which adopts aerogel as Cherenkov radiator. In particular this detector employs a novel method to increase the number of detected Cherenkov photons: two 2 cm-thock layers of aerogel with different refractive indices ($n_1 = 1.045$ upstream, $n_2 = 1.055$ downstream) that

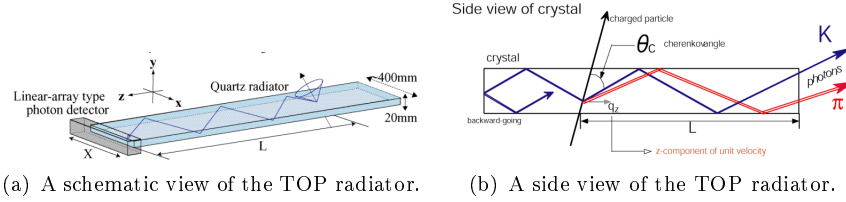


Figure 1.7: TOP detector.

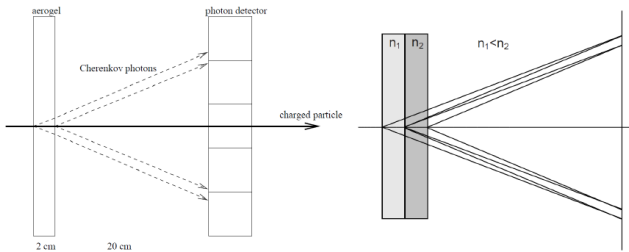


Figure 1.8: ARICH detector.

increase the yield without degrading the Cherenkov angle resolution. A hybrid avalanche photon detector (HAPD) are exploited as single-photon-sensitive high-granularity sensor. Here photo-electrons are accelerated over a potential difference of about 8 KV and are detected in avalanches photodiodes (APD).

The main task of these detector is to improve the K/π separation until 3.5 and 4 GeV/c of momentum, respectively.

1.3.4 Electromagnetic calorimeter (ECL)

The **ECL** is a highly segmented array of tellurium-doped caesium iodide CsI(Tl) crystals assembled in a 3 m long barrel section with a radius of 1.25m, and two endcaps discs located at 2 m (forward) and 1 m (backward). All of them are instrumented with a total of 8736 crystal, covering about 90 % of the solid angle in center-of-mass system. This detector is used to detect gamma rays and to identify electrons in order to separate the latter from hadrons, especially pions.

1.3.5 K_L muon detector (KLM)

It consists of an alternating sandwich of 4.7 cm-thick iron plates and active detector elements located outside the volume of the superconducting solenoid that provides a 1.5 T magnetic field. The iron plates serve as the magnetic flux return joke for the solenoid. They also provide 3.9 interaction lengths or more of material, beyond the 0.8 interaction lengths of the calorimeter, in which K_L^0 mesons can shower hadronically. The active detector elements have been chosen in order to cope with the reduction of the detector efficiency under the SuperKEKB background rates: resistive plate chambers (RPCs) for the outermost active layers, and scintillator strip, with wavelength-shifting fibers,

readout by silicon photomultipliers (SiPMs) in the two innermost layers of the barrel region and for the endcaps regions.

1.3.6 Trigger system

The trigger system of Belle II has a non-trivial role to identify events of interest during data-taking at SuperKEKB, where high background rate are expected. This system is composed of two levels: a hardware-based low-level trigger (L1) and a software-based high-level trigger (HLT), implemented in the data acquisition (DAQ) system.

- **L1:** has a latency of $5 \mu\text{s}$ and a maximum trigger output rate of 30 kHz, limited by the read-in rate of the DAQ.
- **HLT:** is a key component of the DAQ, used to fully reconstruct events that passed the L1 trigger selection. It has to reduce online event rates to 10 kHz for offline storage and it must identify track regions of interest for PXD readout in order to reduce data flux. It fully recreates events with offline reconstruction algorithms, using all detectors information except for the PXD.

1.4 Current state and perspectives of data taking

As we already said, Belle II has reach the world record luminosity with $L_{MAX} = 0.47 \times 10^{-35} \text{ cm}^{-2}\text{s}^{-1}$ in June 2022. In further perspectives, the target is to achieve a new record with $L = 6 \times 10^{-35} \text{ cm}^{-2}\text{s}^{-1}$ and to increase the integrated luminosity from 428 fb^{-1} (actual value, starting in 2019) to 50 fb^{-1} .

In order to accomplish the fixed(established) goals mentioned above, an upgrade not only of the vertex detector but of the whole experiment is necessary, among several reasons, to cope with a more complex circumstances due to the increased luminosity, which undermine its proper functioning.

Therefore a three-phase program is envisaged (considered):

- **short term:** year 2022. Long Shutdown 1 (LS1) is planned for approximately 15 months starting in July 2022, to install a complete pixel detector (PXD). Was it done?
- **short term:** approximately year 2026-27. Long Shutdown 2 (LS2) will probably be needed for the upgrade of the Interaction Region (IR) to reach a new luminosity target $L_{peak} = 6.5 \times 10^{-35} \text{ cm}^{-2}\text{s}^{-1}$. A new Vertex Detector might be required to accommodate the new IR design, and other sub-detector upgrades are possible.
- **long term:** years > 2032 . Studies have started to explore upgrades beyond the currently planned program, such as beam polarization and ultra-high luminosity, such as L_{peak} in excess of $1 \times 10^{-36} \text{ cm}^{-2}\text{s}^{-1}$. While the beam polarization has a concrete proposal, for ultra-high luminosity studies have just started.

At time of writing we are in the period of a long shut-down (LS1), last since June 2022 and the restart of data taking is planned at the beginning of 2024.

2. TJ-Monopix 2

In the previous chapter we have seen the fundamental steps that had lead to the development of the CMOS MAPS sensors thechnology and the history of their many different prototypes.

Here we will go through the main features of TJ-Monopix 2, which represents the improvement of its predecessor TJ-Monopix 1, conceived(designed) to address efficiency degradation after irradiation. The characterization of the chip has crucial consequences in the VTX upgrade program and therefore in the evolution of the OBELIX (sensor).

The chip W14R12 (2.1 on the following page) wihch is one of the matrices tested during the Test Beam in Desy (July 2022) has been fully characterize in Pisa and in particular several aspects have been analyzed, among which:

- TOT calibration by internal charge injection;
- characterization with radioactive sources;
- systematic study of different registers settings in order to operate the chip with lower thresholds;
- investigation of an important issue with cross talk, due to digital signal from the readout, discovered operating at lower threshold (below $250 e^-$).

This well-structured study returned relevant results which have helped in TestBeam data reconstruction and in the simulations SW(???) of the upgraded VTX with CMOS MAPS devices.

2.1 Matrix and flavors

Tj-Monopix 2 is the next generation small collection electrode DMAPS prototype in TowerJazz 180 nm. The need to create a sensor capable to mantain high efficiency even after irradiation, required improvements compared to Tj-Monopix 1 in two important fields: a lower operating threshold and different pixel layout to increase charge collection efficiency all over its area, especially in the corners.

To achieve these goals, a different front-end in pixel circuit was implemented and a lot of efforts have been focused on optimizing pixel layout in order to reduce its size which has been decreased to $33.04 \times 33.04 \mu m^2$. As a matter of fact we have seen in (REFERENCE) that pixel's diensions are critical to accomplish faster charge collection across all active area, increasing the lateral

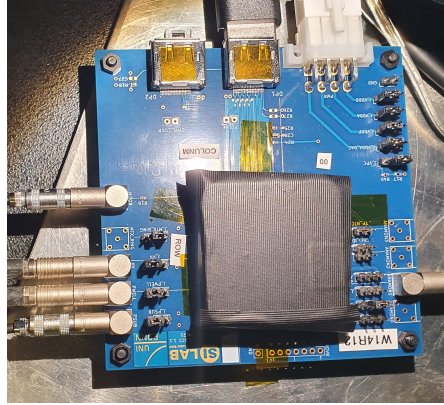


Figure 2.1: The W14R12 chip tested during the Test Beam in Desy.

electric field. For this reason it was necessary a special effort to design and create a smaller pixel but still adequate to embody the full digital readout . All of this required to work at the technology density limit and also further modification at the circuit design, such as single ended data transmission in order to reduce the column-bus width.

2.1.1 Flavors

The prototype is a $2 \times 2 \text{ cm}^2$ pixel matrix which consists of 512x512 pixels and all of them are designed with a reduced deep p-well geometry (RDPW) because as it was demonstrated during the testing of TJ-Monopix1, this type of structure has a superior charge collection properties compared to full deep p-well coverage (FDPW) (figure 2.2). The total active area of the matrix is approximately 286 mm^2 .

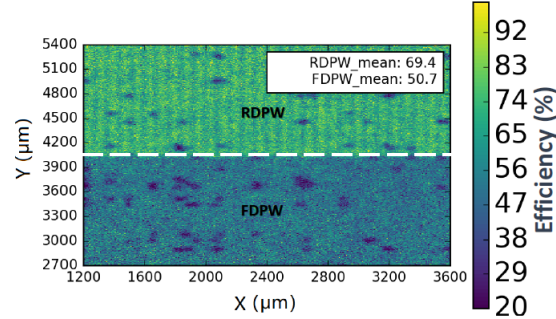


Figure 2.2: Detection efficiency map of a TJ-Monopix1 chip with $25 \text{ }\mu\text{m}$ p-eпитaxial layer that has been irradiated to $10^{15} \text{ }n_{eq}/\text{cm}^2$ NIEL.

As we can see in figure 2.3 on the facing page, the matrix is divided in four sectors, named **flavors** that implement different variation of the front-end circuit. In the first two flavors the collection electrode is DC-coupled directly with the readout electronics, the continuous baseline reset is implemented by a for-

ward bias diode and they differ for the pre-amplifier circuit design. The second flavor, named **Cascode FE**, includes an extra cascode transistor that increase the pre-amplifier gain and results in 50% reduction of the threshold dispersion compared to the first flavor, the **Normal FE**. The other two flavors consist of AC-coupled pixels (through a metal-oxide-metal MOM capacitor) [with front-side HV biasing] and in particular the **HV-Cascode FE** also incorporate the aforementioned pre-amplifier variation. AC-coupling allows to apply an high positive bias voltage (HV) to the collection electrode, but at the same time it also causes signal losses mainly due to the additional parasitic capacitance introduced at the sensitive input node.

The BCID bus width has been increased to 7-bits due to higher gain and ToT slope with respect to Tj-Monopix 1.

It's worth mentioning here that the large column height (approx. 17 mm) due to large matrix area and the aggressive column-bus routing (which refers to the minimum line width and spacing) because of the smaller pixel size (always with respect to TJ-Monopix 1) generated a significant signal transmission delay due to the RC low pass filtering effect of the long metal wires. Consequently a special circuit has been planned(designed) that adds a variable delay to the hit pulse across the column that matches that of the BCID signal.

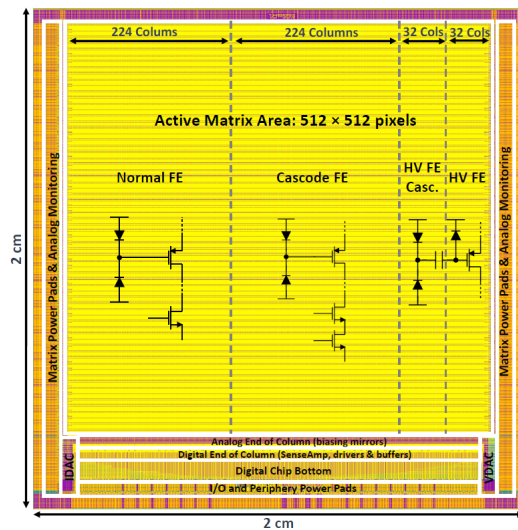


Figure 2.3: The layout of the TJ-Monopix2 prototype divided in four different flavors: **Normal**, **Cascode**, **HV-Cascode** and **HV FE**.

2.1.2 Pixel design

VEDI

The 2×2 pixel core layout, shown in figure ?? on page ?? is fully optimized and is designed in order to share as much functionality as possible between the four pixels. The analog area incorporate the front-end circuit, the 3-bit threshold tuning DAC and the pixel configuration registers. The digital region

is composed by the 7-bit LE and TE memory (14 SRAM cells per pixel), the 10 bit address ROM (2 bit for the pixel position inside the core and 8 for the group address), the readout control logic and the hit delay circuit that is used to correct for the BCID propagation delay. Two different token signal are used to set the priority of the pixels during the readout: the fast one that propagates across the double column established the priority between the cores and the local one, which arbitrates the reading order of the four pixels inside each core.

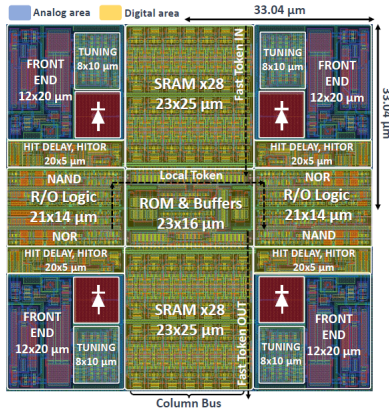


Figure 2.4: Layout of a TJ-Monopix 2 2x2 pixel core. In blue the analog area and in yellow the digital one.

2.1.2.1 Improved front-end circuit design

As we have seen above, there are two variations of the front-end circuit, "normal" and "cascode" type. The latter in particular includes an extra cascode transistor which increases the pre-amplifier gain and consequently reduces the threshold dispersion.

Moreover in TJ-Monopix 2 it was preferred to incorporate a simple diode to reset the input node instead of a PMOS transistor, which was the technology implemented in TJ-Monopix 1. A side effect of this choice is that the relationship between charge injected and the ToT of the detected signal is not linear anymore, because the diode is a not linear element and its discharge rate also depends on the collected charge. Indeed in the following analysis it was necessary to fit the ToT trend with a more complex function. But at the same time, the advantages are its simplicity (p^+ diffusion within the n-well collection electrode) and also the fact that it allows to increase radiation tolerance to TID effects, which was one of the key working area in the upgrade of the sensor, in order to design a final(conclusive) prototype to employ in the experiments subjected to high radiation doses.[pag 153???

In the last two AC-coupled flavors are implemented the same improvements, but here the different coupling provokes an important loss in the collected charge, as verified during the testing phase of TJ-Monopix 1 (50% losses), due at most to additional parasitic capacitances. Thus (THerefore) a lot of (many) efforts have been made to improve this aspect, working on the coupling capaci-

tor values. It is reach a signal loss of 41.5%, which is an enhancement (progress) with respect to the predecessor.

2.2 Threshold and noise

In order to achieve the absolute calibration of the whole matrix, the response of each pixel has been characterize by means of the internal charge injection.?????

The hit injection circuit included in TJ-Monopix 2 is similar to the one of TJ-Monopix 1, shown in figure(????). It allows to inject artificial hits through an injection capacitance C_{inj} connected at the collection electrode, which is equal to 230 aF for both the DC and AC coupling FE. The injected charge is almost linear with the injection pulse amplitude (set by the two registers " V_L " and " V_H ", like $\Delta V_{inj} = V_H - V_L$). Moreover the injection step is finer compare to the one of TJ1 because of the higher voltage DAC resolution, in fact LSB (*Least Significant Bit*)=7.03 mV. The injected charge Q_{inj} can be calculated from:

$$Q_{inj} = \frac{230 \text{ aF}}{q_{e^-}} \cdot \Delta V_{inj} = 1.4375 \frac{e^-}{mV} \cdot 7.03 \frac{mV}{DAC \text{ unit}} \approx 10.1 \frac{e^-}{DAC \text{ unit}} \quad (2.1)$$

Eventually this value has been used to convert the information of the injected charge from DAC unit to electrons unit useful for further analysis.

The four flavors have been separately analyzed to be able to study their main difference concerning their performance and features, but the same method, called *s-curve method*, explained below has been used.

2.2.1 S-Curve method

In order to obtain the threshold and noise values for all pixels, each one of them has to be injected an arbitrary number of times (100 times in this work) for each value of the injection pulse between a minimum voltage (value), chosen setting the chip register "**VL**" and a maximum volatge (value) set by the "**VH**" register, with a step of 1 DAC unit this is also adjustable). These two levels are provided by the voltage DAC.

So for each injection pulse height, the mean of 100 injection output are considered and it represents one data in the plot. In this way plotting the average number of detected hits in function of the injected charge, the typical curve better known as "*S-curve*" is reconstructed. It can be fit with the *Cumulative Distribution Function (CDF)*:

$$CDF(Q) = \frac{1}{2} \cdot \left(1 + \operatorname{erf}\left(\frac{Q - \mu}{\sigma\sqrt{2}}\right) \right) \quad (2.2)$$

from which the value of the threshold is evaluated considering the value of the injected charge at half of the curve's maximum height, so the parameter μ obtained from the fit and the noise instead is evaluated from the fit parameter σ . $\operatorname{erf}(x)$ is the Gauss error function.

Specifically plotting the number of hits observed on each pixel divided by the total number of injections, for each injected charge, the half height corresponds to a charge value for which the pixel detects 50 hits of 100 injected and so when

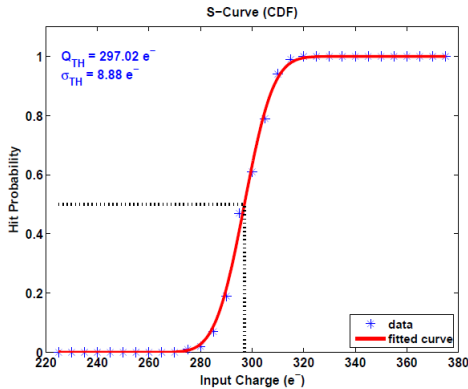


Figure 2.5: An example of the S-Curve fitted by the CDF to evaluate threshold and noise.

it has an occupancy of 0.5. In figure 2.5 is shown an example.

This method allows to study the noise and threshold of all pixels and also the threshold dispersion across an entire FE.

In the following are reported the results of this study for the flavors of all matrix, injected a charge gradually increasing from 0 to 140 DAC ($\approx 1414 \text{ e}^-$ adopting the conversion factor in equation 2.1)

2.2.1.1 Normal FE

The first flavor of the matrix is the **Normal FE**, which consist of 512 rows and 224 columns for a total of 114.688 pixels. The chip registers have been set with the same values used during the Test Beam at Desy (July 2022) which are different for the DC and AC-coupling case. They are known as "**GOE settings**" and they are reported in table 2.1 on the next page, where are also added the different biasing voltages used to power (up) the chip.

Using this setting, none of the pixels were noisy and so it wasn't necessary to use any mask. In figure 2.6 on the facing page are plotted all the s-curves of the all well-functioning Normal flavor pixels. The width of the plot is a first indication (manifestation, symptom) of the threshold dispersion of the whole flavor.

The threshold and noise distributions obtained injecting all pixels as explained above, have been fitted with a gaussian distribution and they are shown in figure ?? with their maps, too.

2.2.1.2 Cascode FE

Cascode FE is the second flavor and like **Normal FE** it consists of 512 rows and 224 columns for a number of total pixels equal to 114.688. For this flavor the same procedure of Normale FE has been followed and also the same values' registers (table 2.1 on the next page) have been used. There were not find noisy pixels. In figure ?? on page ?? the S-curves of all pixels are shown.

Registers	Normal/Cascode FE ($P_{SUB}/P_{WELL} = -3$ V)	HV/HV-Cascode FE ($P_{SUB}/P_{WELL} = 0$ V, HV = +5 V)
I_{THR}	64	30
I_{BIAS}	50	60
V_{RESET}	143	100
I_{CASN}	0	8
V_{CASP}	93	40
V_{CASC}	228	228
I_{DB}	100	100
I_{TUNE}	53	53
V_{CLIP}	255	255
I_{COMP}	80	80
I_{DEL}	88	88
I_{RAM}	50	50

Table 2.1: Settings of the main registers used for all flavors (W14R12 chip) during the Test Beam in Desy.

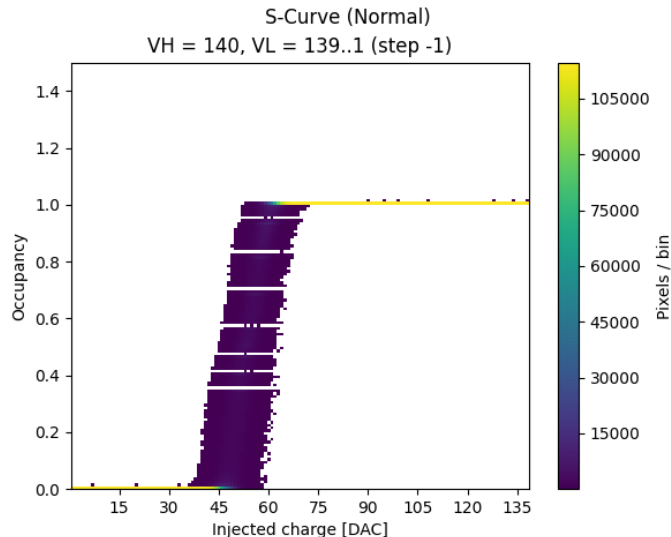


Figure 2.6: S-curves of all pixels of the Normal FE with an injection pulse of 140 DAC.

The fit of the threshold and noise distributions and maps instead, are shown in figure ?? on page ??.

2.2.1.3 HV-Cascode FE

The third flavor is **HV-Cascode FE** where HV stands for **High Voltage** and it is formed (counts) of 512 rows and 32 columns for a total number of pixel equal to 16384. Also for these last two flavors, the main chip registers are set with the same values tested and used during the Test Beam (@Desy) (but different from

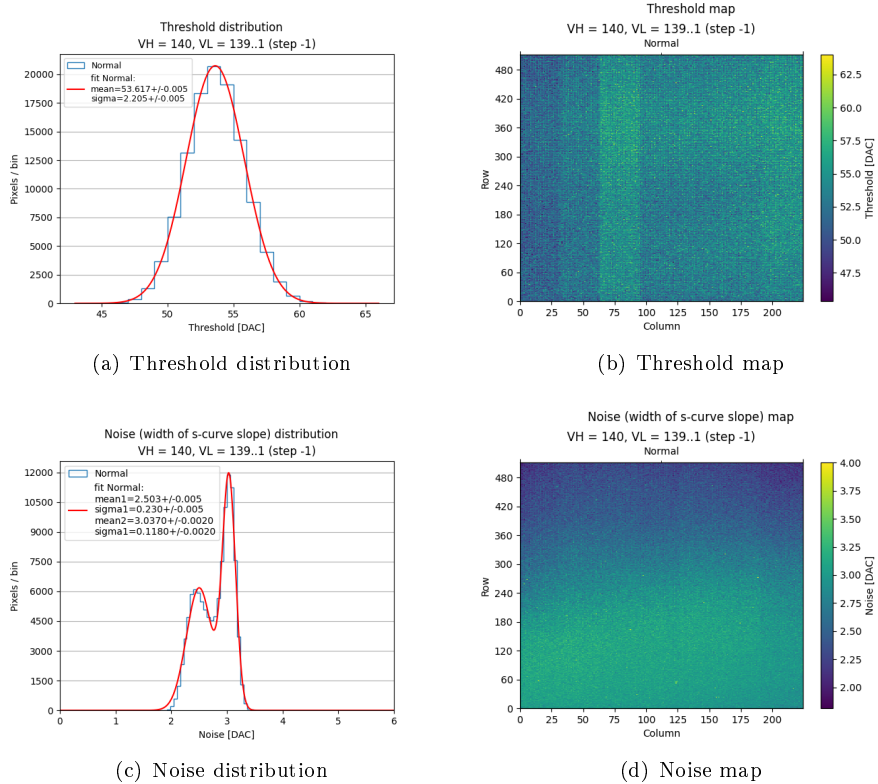


Figure 2.7: Normal FE.

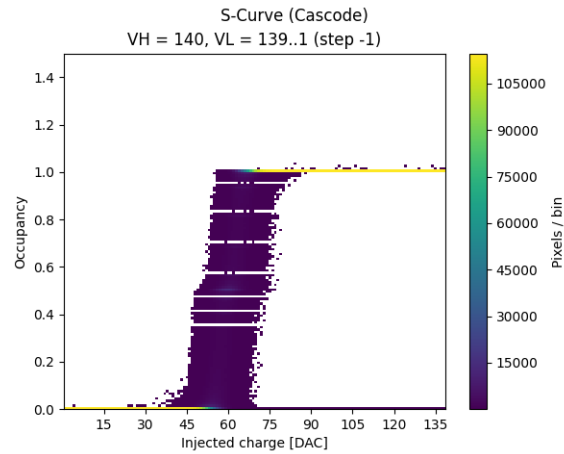


Figure 2.8: S-curves of all pixels in the **Cascode** flavor with an injection pulse of 140 DAC.

those used for the first two flavors). They are reported in table on page ?? .

As we can see from the plot of the alle S-curves in figure on page 24, there

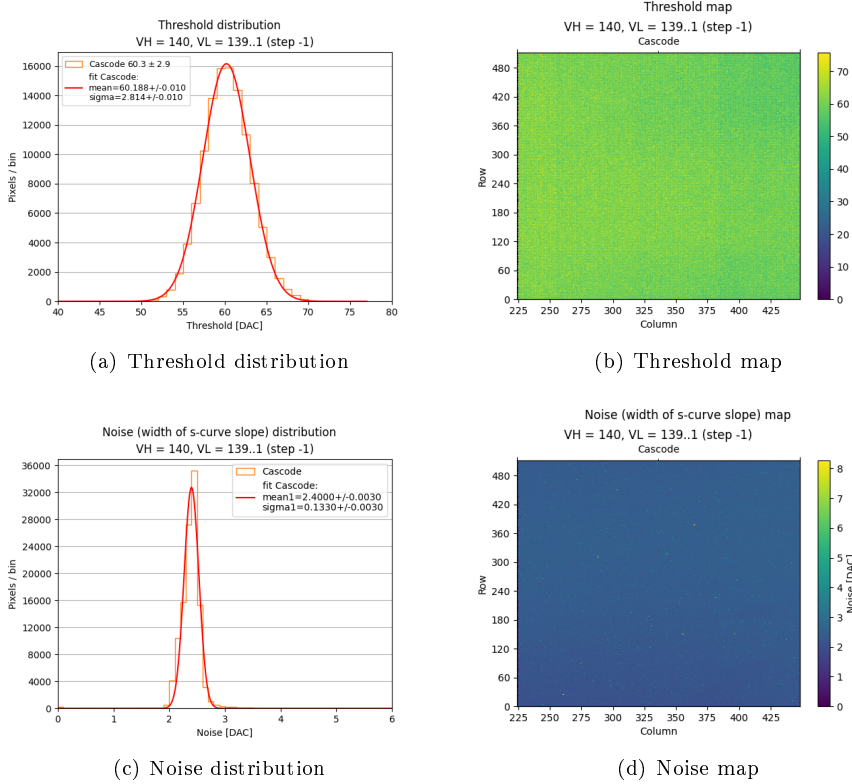


Figure 2.9: Cascode FE.

were a lot of noisy pixels with these choices of values' registers, but at this stage of measurements they were not masked. As a matter of fact along the y-axis of this plot is displayed the occupancy and when this value becomes higher than 1, it means that the pixel detects more hits than the injected ones, so it could be identified as "*"noisy pixel*" (because it results active regardless of the charge injection)".

In figure 2.11 on the following page are shown the fit of the threshold and noise distributions.

2.2.1.4 HV-Normal FE

The fourth and last flavor is the **HV-Normal FE** which consists of 512 rows and 32 columns for a total number of pixels equal to 16.384. The main registers have been set with the values reported in table on page ???. In figure on page ??, the S-curves of all pixels in the flavor. Also here we can see that there were some noisy pixels unmasked. Moreover, in this final flavor, the last 16 columns were not working (visible in the maps in figure on page ??) and as a matter of fact they had returned a peak of threshold near the value 0, which is excluded from the threshold distributions plots.

So actually in this part of the matrix, the real number of pixels studied was the half of the total, such as 8192 pixels.

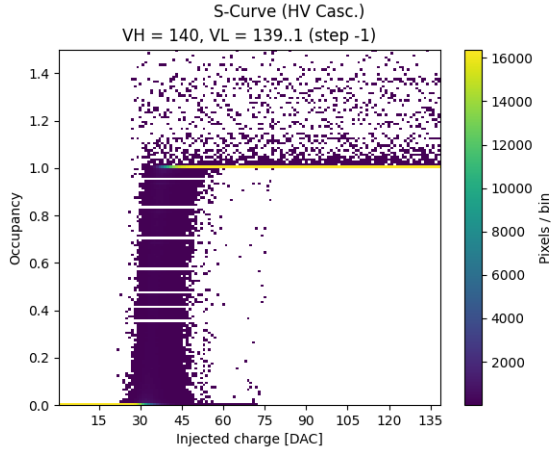


Figure 2.10: S-curves of all pixels in **HV Cascode** flavor with an injection pulse of 140 DAC.

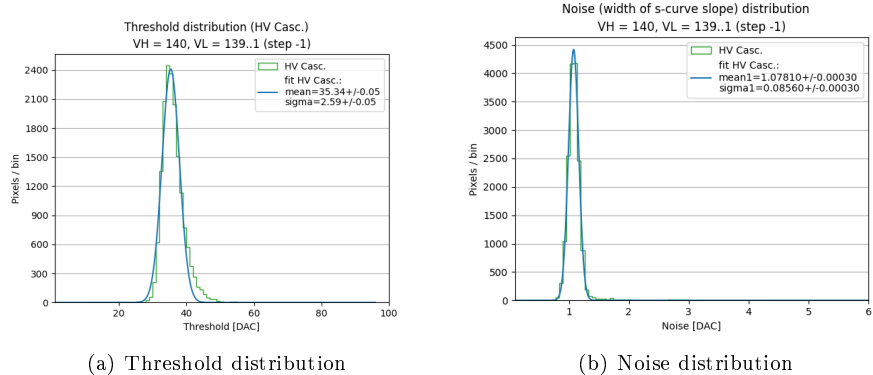


Figure 2.11: HV Cascode FE.

In figure 2.13 on the facing page the fit of the threshold and noise distributions.

At last in figure on page ?? the threshold and noise maps of the whole HV flavor.

As we will see in the following (section REFERENCE), the atypical s-curves in HVs flavors have been the first hint(evidence) of the cross-talk problem (section REFERENCE) tied to a lower global threshold in these sectors with TB settings.

2.2.1.5 Summary Table

In table on page ?? a summary of results for threshold, noise and threshold dispersion of all FE.

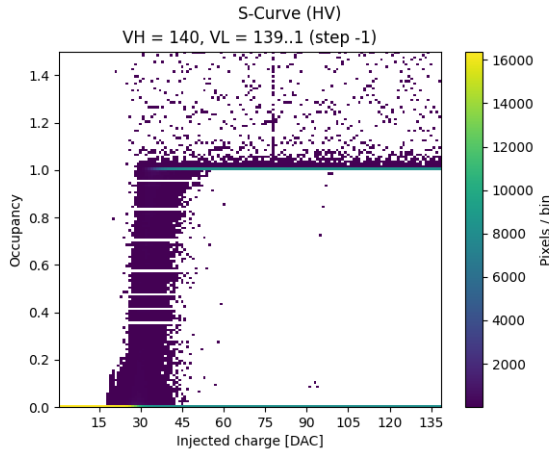


Figure 2.12: S-curves of all pixels in **HV Cascode FE** with an injection pulse of 140 DAC.

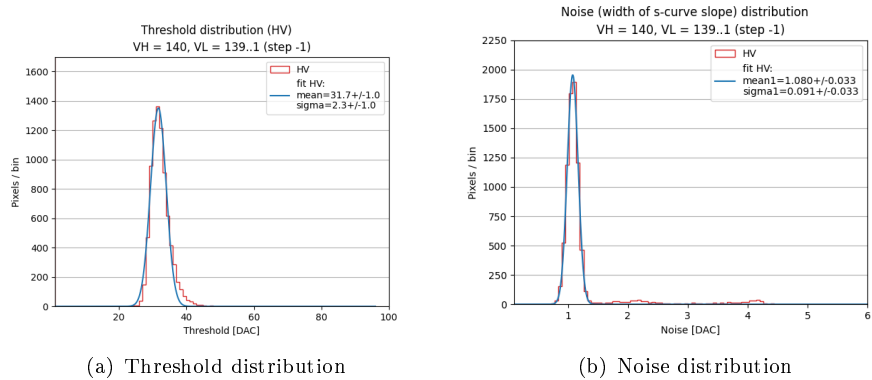


Figure 2.13: HV Normal FE.

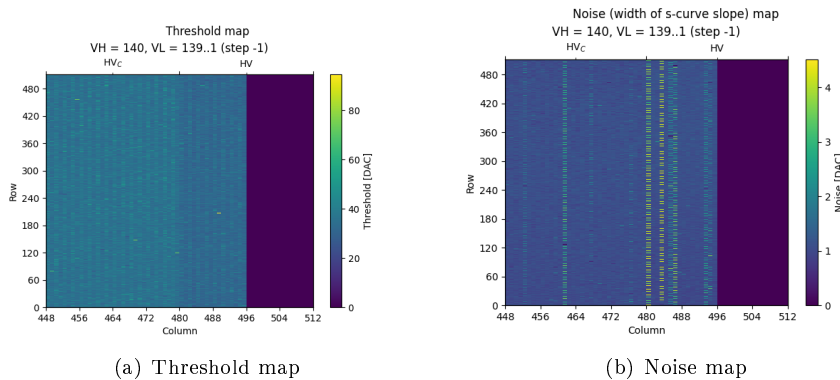


Figure 2.14: HV's FE.

Front-End	Threshold [e^-]	Threshold dispersion [e^-]	Noise [e^-]
Normal	53.62 ± 0.01	2.21 ± 0.01	2.503 ± 0.005
Cascode	60.19 ± 0.01	2.81 ± 0.01	3.037 ± 0.002
HV - Cascode	35.34 ± 0.05	2.59 ± 0.05	2.400 ± 0.003
HV	31.70 ± 0.10	2.30 ± 0.10	1.0781 ± 0.0003
			1.080 ± 0.033

Table 2.2: Summary table of threshold and noise values for all flavors of the W14R12 chip.

2.2.2 Threshold dispersion and tuning

Despite its predecessor, Tj-Monopix 2 is equipped with a circuit which allows the *threshold tuning*. In other words it can adjust every pixel threshold, even if only by few DAC, in order to have a global threshold on the matrix as uniform as possible, or in any case a dispersion as small as possible, especially after irradiation. We have already noticed that (took a look to) (2.4 on page 18) the analog part of the in-pixel front-end that includes the 3-bit threshold tuning DAC, which not only improves the global threshold dispersion across the pixels, but also solves the issue with the unintentionally masked ghost pixels, reducing the noise even more. This system has been design in order to decrease the some effects that affected the threshold disperision like systemstics (for example, related to biasing), process and temperature variations and radiation damage.

Threshold trimming of each (individual) pixel is performed with the help of a tuning DAC (TDAC), shown in figure 2.15 on the facing page. In particular this component controls the discriminator active load (comparison?) current I_{DISC} which is partly(?) responsible of the pixel threshold. It works as an analog multiplexer (consisting of simple PMOS transistor switches), which selects one of seven $I_{DISC,n}$ lines generated by the main 8-bit biasing DAC. So the possble value of the final I_{DISC} is given by the sum of two contributions:

$$I_{DISC} = I_{DISC,coarse} + (TCODE - 1) \cdot I_{DISC,fine}, \quad \text{where} \quad 1 \leq TDAC \leq 7 \quad (2.3)$$

$I_{DISC,coarse}$ is the current sets by the main(raw?) value of threshold, resulting by the setting of the main registers which are responsible for it. $I_{DISC,fine}$ is the current selected by the fine tuning step (TDAC) and it depends on the 3-bit tunning code that is stored in the in-pixel tuning memory latch (the in-pixel configuration memoty). **TCODE** is the decimal representation of the TDAC code.

For example if the 3-bit DAC are set to "111", the decimal representation is 8 and the fine tuning provide a current $I_{DISC,7}$, which corresponds to the highest threshold. If the 3-bit are set to "010" the corresponding TCODE is 2 and the current $I_{DISC,1}$ is provided that set the lowest threshold possible around the central value $I_{DISC,coarse}$. The particular combnation "000" instead (TCODE = 0) masks the pixel by disabling the discriminator, without affects the functioning(operation) of the others.

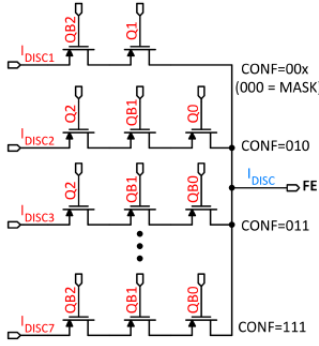


Figure 2.15: Schematic of 3-bit tuning DAC (TDAC)

2.2.2.1 Results from fine tuning

It has been trying to apply the fine tuning method to level out the threshold of some pixels as much as possible.

Results from measurements done later (Ludovico talk TREDI) pre and post

2.3 ToT calibration with internal injection

As it has been pointed out in the previous, choosing to use a simple diode instead a PMOS transistor as reset input baseline element, increases the tolerance to TID radiation but at the same time it implicates a non-linear relationship between the injected charge and the ToT. For this reason, one of the target of this analysis consisted to fit the trend (?) Q_{inj} vs. ToT, in order to obtain the absolute calibration of the whole matrix.

2.3.1 Injection circuit issues

In carrying out the measurements mentioned above, we started to noticed some issues with the injection circuit, which seemed to limit its working range. As a matter of fact the height of the injection pulse is expected to grow linearly increasing the value of charge to be injected. It actually happened up to a value of (about) ≈ 140 DAC, but for higher quantities of injected charge, the circuit seemed to increase not only the height of the signal, but also the threshold by a certain amount of ΔV (or equivalently of ΔQ , related by the conversion factor reported in REFERENCE). Moreover, for injection height grater than 200 DAC, only the threshold grows, without increasing the actual injected charge in any way.

We come to the conclusion that the grows of the threshold was artificial and due to the failure of the injection circuit.[?]

However as we have seen in the previous section (reference), the threshold depends on the settings of the chip registers and it can't be influenced by the injected charge, otherwise the whole response of the chip would be chaotic and it would not be reliable to take precise measurement of the impinging particles.

A method (recipe) has been therefore devised to obtain a reliable values of threshold and ToT up to a value of 170 DAC of effective (actual) charge injected. Moreover the characterization of the function to describe the Q_{inj} - ToT relationship has allowed also to extrapolated ToT values in the forbidden region of charge by the internal injection circuit issue (above $\approx 1717 e^-$), that usually corresponds to the emission peaks of the radioactive sources available in the laboratory.

2.3.2 Time Over Threshold (TOT) curves and fit

The function chosen for this purpose is:

$$y(x) = a \cdot x + b - \frac{c}{x - t} \quad (2.4)$$

with a , b , c and t free parameters and where the y represents the ToT corresponding to a precise value of collected charge, express by x .

Actually we know that the ToT distribution starts to grow near the threshold, so a random parameter among them, could be computed in function of the threshold value estimated from the previous measurements, explained (shown, described) in section 2.2.1.

In particular knowing that $y(x_{th})$ must be equal to 0, that is the ToT at the value of the threshold, it can be imposed:

$$0 = a \cdot x_{th} + b - \frac{c}{x_{th} - t} \Rightarrow c = x_{th}^2 \cdot a + x_{th} \cdot (b - a \cdot t) - t \cdot b \quad (2.5)$$

In this way the number of parameters to fit is reduced.

So the same data collected in the previous measurements of thresholds have been used to fit the ToT curves of all pixels for each frontend, so the registers are set in according to the "GOE" settings (2.1 on page 21 for Normal and Cascode FE and ?? on page ?? for HV's). In table 2.3 are reported the value of the threshold considered for each one of them (so that) to extrapolate the value of the parameter c and the results of the fit for all parameters. In figure 2.16 on the facing page the results obtained for all Normal, Cascode and HVs FE. The parameter c is chosen only for simplicity of calculation.

	Normal	Cascode	HV Cascode	HV
<i>threshold [DAC unit]</i>	53.62	60.19	35.34	31.70
<i>a</i>				
<i>b</i>				
<i>c</i>				
<i>t</i>				

Table 2.3: Threshold and parameters obtained from the fit of ToT curve for each frontend.

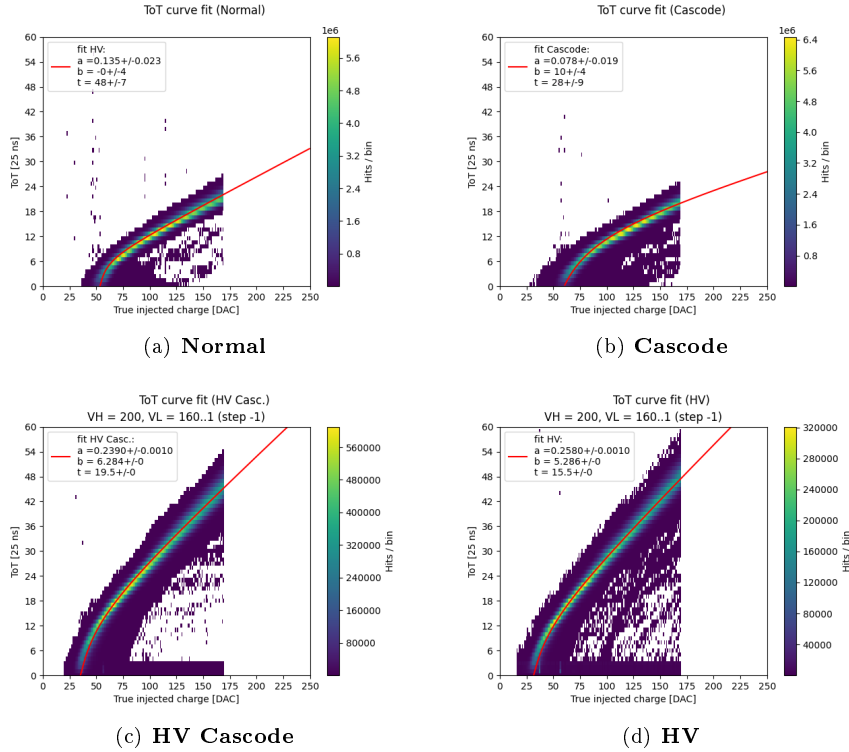


Figure 2.16: ToT curves fit for all frontend.

2.4 Response to radioactive source and absolute calibration

The absolute calibration of the matrix consists in characterizing the signal response (conversion gain?) of pixels for each FE. By the means of the Q_{inj} - ToT fit (section 2.3.2), it is possible to extrapolate (deduce, estimate) the value of the ToT of the signal induced for whatever collected charge. At this point then, three (or four) different X-rays radioactive sources were used to study the signal spectrum and the response time of the matrix, with emission lines from 6 to 60 KeV (1600 to 16000 e-).??? In fact the known energies of the sources emission spectrum (so that the charge released in the matrix from particles emitted in decays) allow to compare the spectra obtained irradiating the chip, with the expected value of their peaks. [Only the events in which all charge induced is collected in a single pixel are a part of the peaks reconstructed by the chip.] Moreover these radioactive sources allowed to extend the ToT calibration for(at) higher value with respect to the limit imposed by the saturation of the internal injection circuit (section 2.3.1). In table 2.4 on the next page are shown the emission energies of the sources employed, that it was possible to see with the chip under test.

[Considering that the average energy necessary to produce an electron/hole pair in silicon is 3.65 eV, it is possible to convert the peak energies in a mean

value of electrons released by the means of equation on this page. So in the table are reported also the equivalent emission in electrons, which will be useful further.]

$$N_{e^-} = \frac{E [eV]}{3.65 \left[\frac{eV}{e/h \text{ pair}} \right]} \quad (2.6)$$

Source	Energy γ [KeV]	Equivalent charge [e^-]
^{55}Fe	5.9	1616
^{241}Am	13.9	3808
^{241}Am	17.7	4849
^{241}Am	20.7	5671
^{109}Cd	22	6027
^{241}Am	26.4	7233
^{241}Am	59.7	16356

Table 2.4: Emission lines of ^{55}Fe , ^{241}Am , ^{109}Cd sources visible by the sensor.

2.4.1 ^{55}Fe

The ^{55}Fe source decays by **electron capture** to ^{55}Mn . One of the photons emitted in this transition has an energy of 5.9 KeV (K_α) and it produces in turn a photo-electron which deposits an ionization charge of about 1616 e^- in the sensor. All flavors were irradiated with a ^{55}Fe source available in the laboratory (scrivere caratteristiche). In figure 2.17 on the next page are shown the results obtained. Each peak was fitted by a gaussian function, limited in the region of the peak itself. The hump (shoulder, bump) for smaller ToT is a consequence of charge sharing among pixels.

As it can be seen for the HV's FE a cut has been applied only to make clearly visible the emission line because a lot of noisy pixels caused a sharp peak at 0 ToT. As a matter of fact in this flavors there were several columns of non-functioning pixels. In the box of each plot are also reported the results of the fit that will be crucial in the following.

2.4.2 ^{241}Am

The ^{241}Am source has a more complex spectrum (figure 2.18 on the facing page) and not all its peaks can be revealed (detected) by the chip (because of the limited range of ToT available, depending on the bit dedicated to it). The spectrum shows other minor peaks besides the usual intense gamma peaks (59.5 and 26.3 keV) and several characteristic L X-rays from ^{237}Np (20.7, 17.7 and 13.9 keV).

Results are reported in figure 2.19 on page 32. In the case of the first two flavors, it could be possible to fit four peaks of the emission lines. In case of the HV's flavors instead, only three peaks for the HV-Cascode FE and two for the HV.

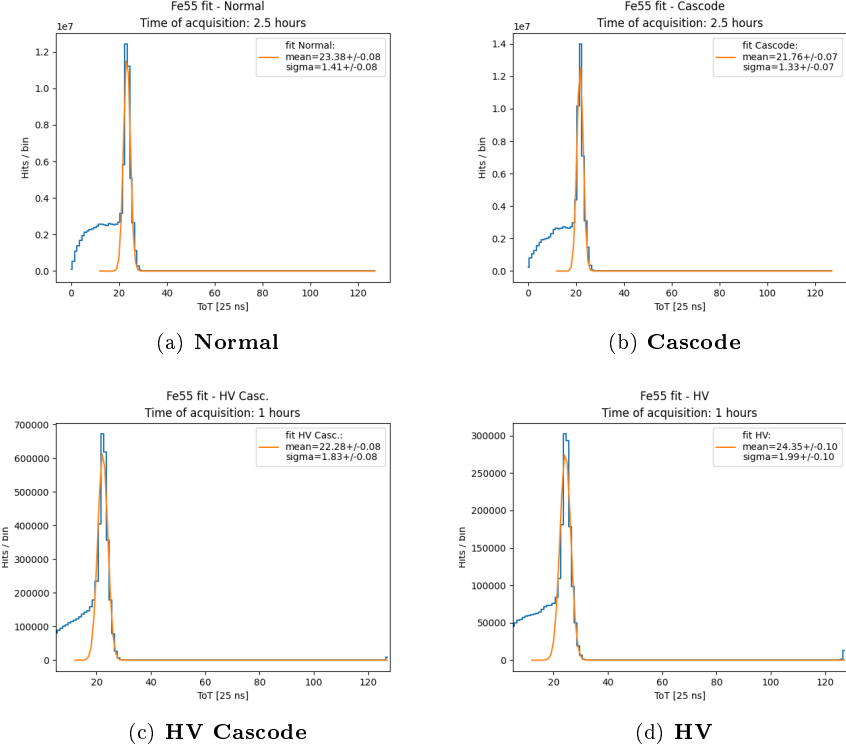


Figure 2.17: ^{55}Fe peaks for all frontends.

As a matter of fact the AC-coupling causes about 41% of signal loss (reference), so they are much less evident and more difficult to fit as isolated peak.

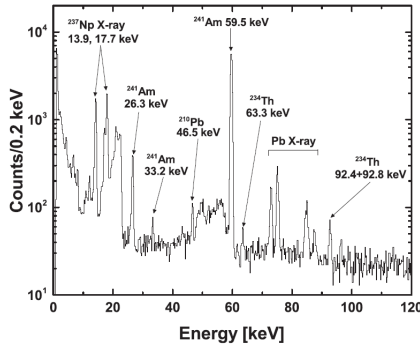


Figure 5. Gamma-ray spectrum of the ^{241}Am source.

Figure 2.18: ^{241}Am γ emission spectrum.

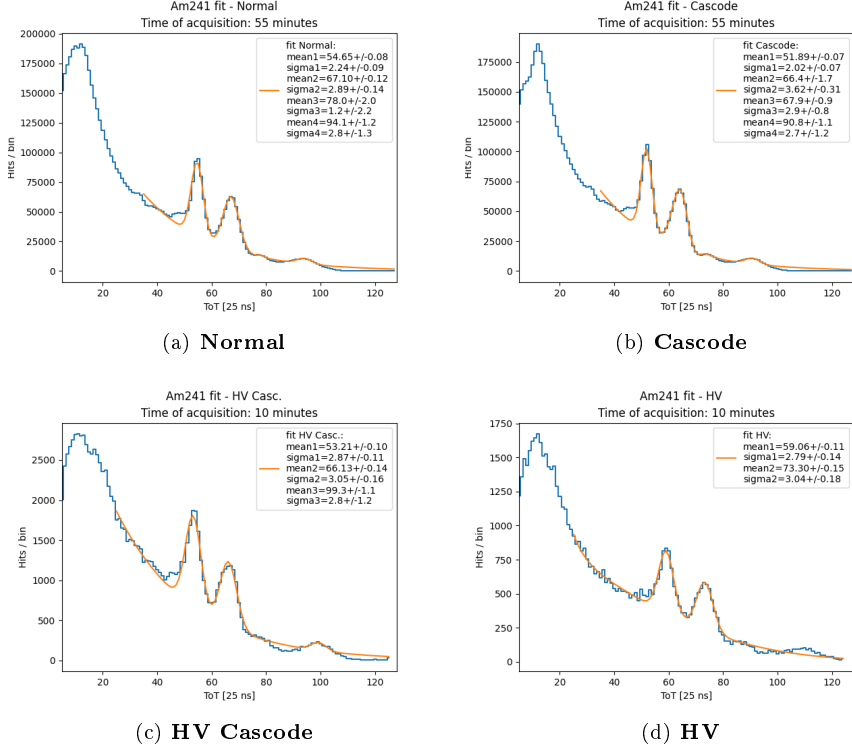


Figure 2.19: ^{241}Am peaks for all frontends.

2.4.3 ^{109}Cd

The third source employed was the ^{109}Cd . This isotope decay in ^{109}Ag by electronic capture, producing a photon of 22 KeV in the transition. In figure ?? on page ?? the results obtained irradiating all FE.

2.4.4 Injection capacitance calibration

Here it's necessary to point out that for iron source more statistics were collected so in this case a complete analysis of each pixel could be done. For the other sources instead, there weren't enough statistics on every pixel so the injection capacitance has been estimated only as a mean value for the whole front-end, just to compare with the results obtained from the iron analysis.

In case of ^{55}Fe source, we managed to fit the emission peak for each working pixel of the whole matrix. The value of the charge corresponding to the ToT peak of the emission line was extrapolated considering the parameters' values obtained by fitting the Q_{inj} - ToT relationship (section on page 28).

Specifically the fit function on page 28 was inverted obtaining:

$$x(y) = \left(\frac{t}{2} - \frac{b}{2a} + \frac{y}{2a} \right) \pm \sqrt{\left(\frac{t}{2} + \frac{b}{2a} - \frac{y}{2a} \right)^2 + \frac{c}{a}} \quad (2.7)$$

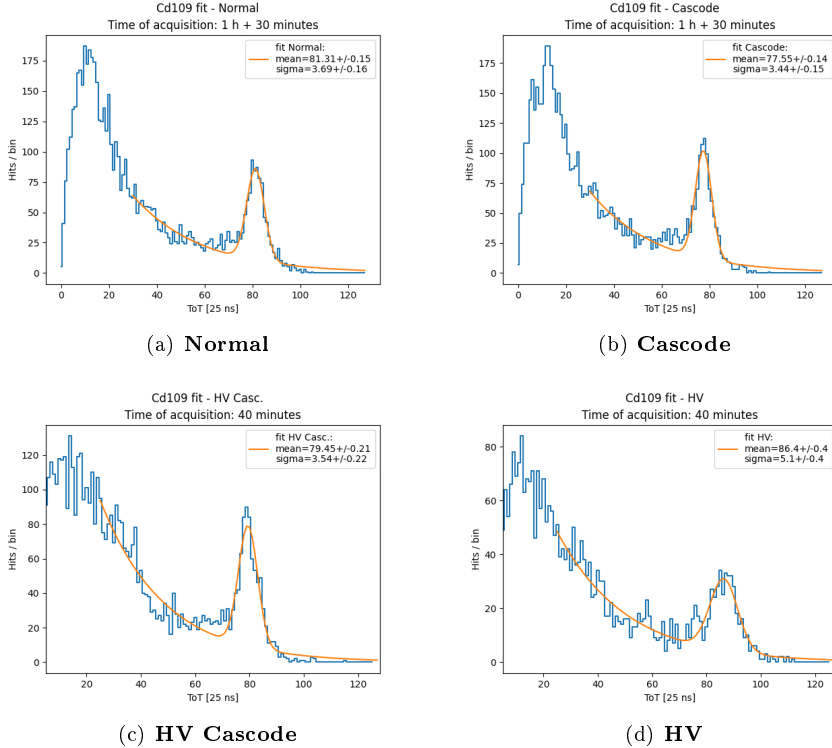


Figure 2.20: ^{109}Cd pekas for all frontends.

where x represents the charge corresponding to the ToT labeled by y .

As shown in table on page 30, the charge released in the sensor (considering that collected from only one pixel) corresponds roughly (\approx , approximately) to $1616 e^-$. Therefore it was possible to calculate (estimate) the conversion factor for each pixel as follows:

$$C_f \left[\frac{e^-}{DAC} \right] = \frac{1616 e^-}{ToT \frac{DAC}{ToT_{unit}}} \quad (2.8)$$

By these steps, a value of the injection capacitance was estimated for each well-functioning pixel. In figure on the following page is reported the distributions of the injection capacitance estimated, fitted by a gaussian function.

[As expected the capacitance of the HV's flavors is much higher than the Normal and Cascode FE? No! It's expected all the same?]

Regarding the other sources, it was impossible to fit the distributions for each pixel due to low statistics. For this reason only a mean value for all flavor could be extrapolate. In table on page 35 the results obtained with the same method used with the iron source, but considering all pixels of each flavor.

Bringing equation on page 19 back to mind, the conversion factors of the flavors are not those expected. In particular for the HV's flavors, this factor is almost the double and it could mean that the injection capacitance is greater than expected. As matter of fact, with respect to Tj-Monopix 1, the prototype

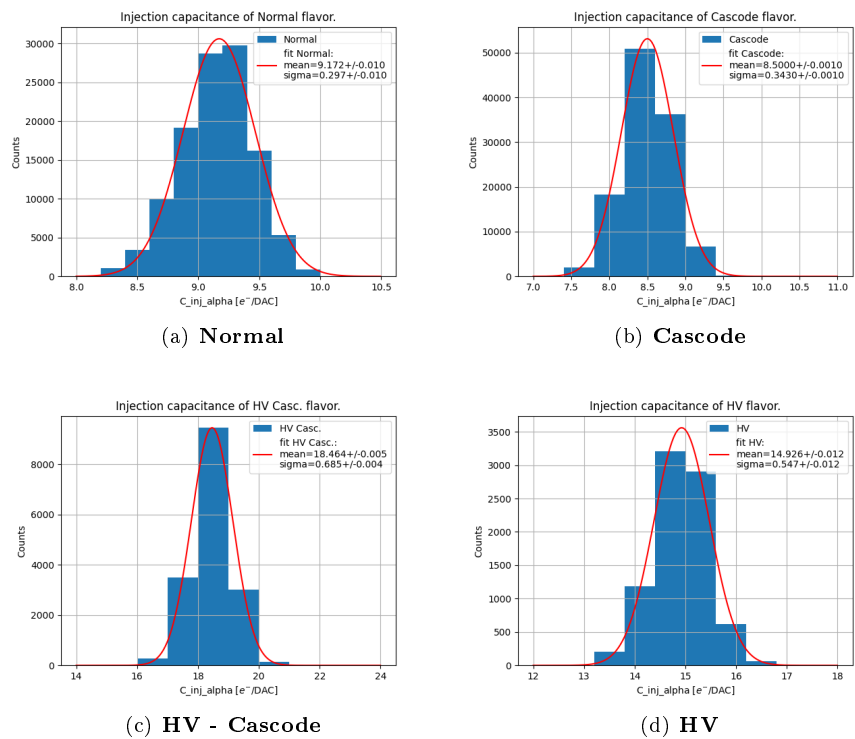


Figure 2.21: Injection capacitance distributions of all FE.

Source peak	C_{Normal}	$C_{Cascode}$	$C_{HVCascode}$	C_{HV}
^{55}Fe (5.9 KeV)	9.37	9.00	19.33	18.56
^{241}Am (13.9 KeV)	8.94	8.91	19.23	18.22
^{241}Am (17.7 KeV)	9.16	8.84	19.59	18.63
^{241}Am (20.7 KeV)	9.15	10.11	-	-
^{109}Cd (22 KeV)	9.32	9.39	20.16	19.6
^{241}Am (26.4 KeV)	9.60	9.61	19.25	-
Mean value	9.26	9.31	19.51	18.75

Table 2.5: Estimation of injection capacitance of all flavors for different source emission peaks.

under test was design in order to have the same injection capacitance for all flavor, equal to 230 aF.

so? Loss of charge?

It's necessary to consider that maybe some measurements were done in different conditions of pressure and temperature?

2.4.5 Check on linearity of tot fit

In the end all emission peaks from the several sources have been plotted for each frontend in order to verify the agreement between their trend and the ToT-Q relationship studied by the internal injection.

At first the charge corresponding to the electrons expected to be released for each peaks, has been calculated with the nominal conversion factor equal to $10.1 \frac{e^-}{DAC}$. As it could be seen from results in figure on the next page there isn't good agreement between data and ToT relationship obtained(learnt) in section on page 28.

After the calibration instead, assuming the average value of injection capacitance calculated in table on page ??, the charge corresponding to the emission peaks have been recalculated and results are shown in figure on page 37.

After(through) the calibration a better agreement is therefore obtained.

2.5 Operation with low threshold

One of the most important target of the chip design is to keep high efficiency even after irradiation damage. All experimental environments in fact (indeed) are exposed to high doses of radiations, so it's crucial to make sure the functionality of the irradiated detectors.

For this reason, many tests were done in order to understand the chip behaviour at lower threshold that allowed to keep(maintain) good value of efficiency. Moreover working at low threshold allowed to detect low charge events due to charge sharing or charge trapping (effect which increased after irradiation), especially in case of thin epitaxial material.

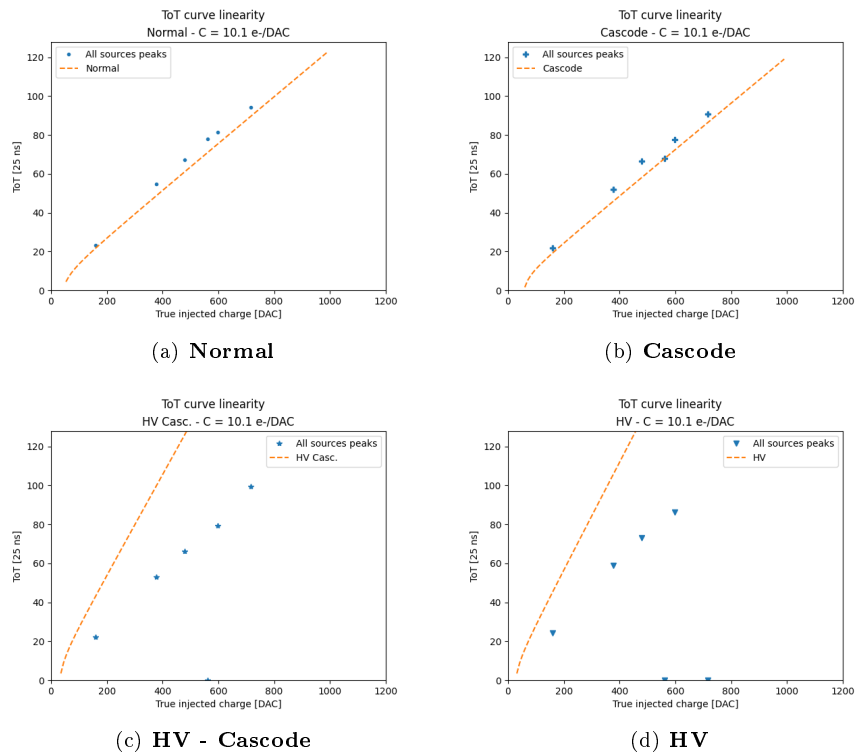


Figure 2.22: ToT linearity of all flavors assuming the nominal(expected) conversion factor equal to $10.1 \frac{e^-}{DAC}$.

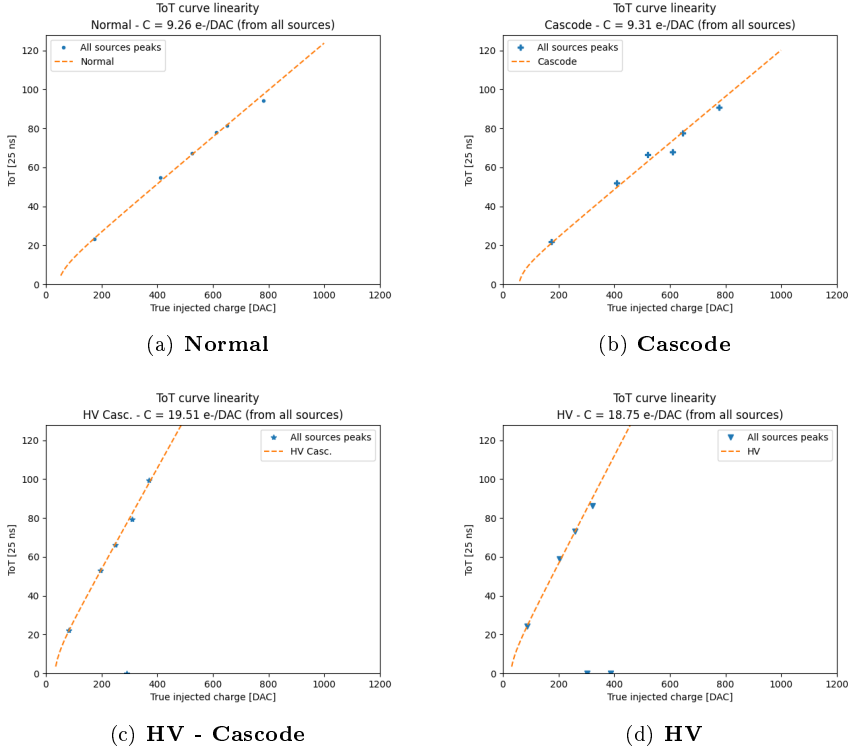


Figure 2.23: ToT linearity of all flavors assuming the conversion factor obtained from calibration for each FE.

2.5.1 Register optimization

As we have seen in section (REFERENCE), there are a lot of registers which control the discriminator threshold and also the readout sequence. So preliminary it was necessary to run some tests exploring their settings in order to operate the chip at(or with) lower thresholds.

Now we will go through the main registers used for this purpose, in order to explain their functionality. There are several dozens of registers but we focused on some of the most important and crucial to set the threshold:

- I_{CASN} : this current is responsible of the output baseline signal[set the baseline of the FE output and change the thr] that goes to the input discriminator. In a few words, higher this value, higher the baseline, lower the threshold and also a little bit the gain. [Vice versa, decreasing this register's value.]
- I_{THR} : it controls the pre-amplifier feedback strength and speed, so it's responsible for the output reset rate. Increasing I_{THR} results to lower gain and faster return to baseline, so higher threshold. In other words increasing this current increases the gain and the time the analog output takes to get back to the baseline and as consequence, it increase a lot

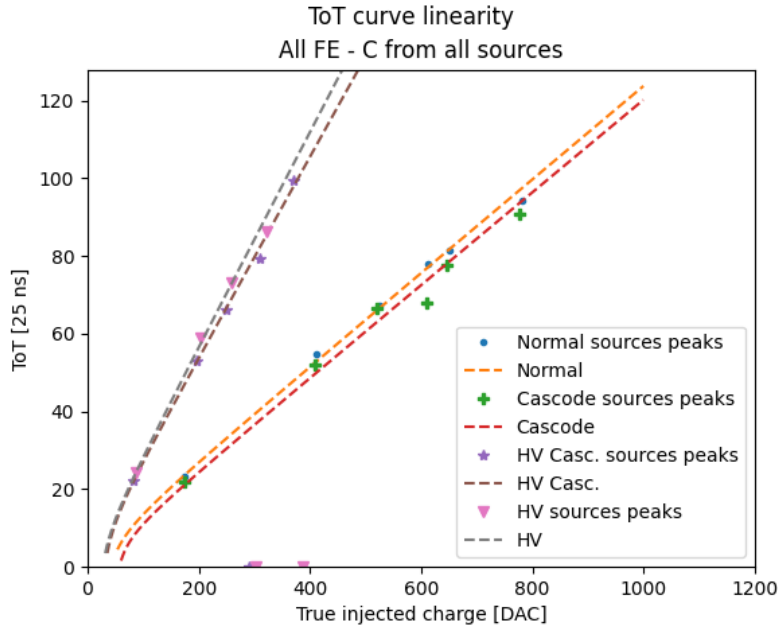


Figure 2.24: Summary of trends.

the maximum value of the ToT. In fact is preferably set I_{THR} to 8nA[in DAC?] in order to avoid high ToT slope.

- I_{DB} :
- I_{TUNE} :
- I_{BIAS} :
- V_{RESET} : dispersion?

2.5.2 Comparison between data and simulation

In the interest of understanding how the settings of the chip influence the threshold's value, several measurements have been taken varying the values of the main registers which are responsible for it. The results are compared with simulations done by Hung Pham (...). [???

2.5.2.1 I_{CASN}

This current is responsible of the output baseline. In a few words, higher this value, higher the baseline, lower the threshold and also a little bit the gain.

In figure 2.25 on the next page, we can see the simulated behaviour of the threshold and the gain, increasing the value of I_{CASN} .

To verify the trend of threshold in particular, three different acquisition have been taken by fixing $I_{THR} = 20, 40, 64$ and increasing I_{CASN} from 0 to 30 DAC, with a step of 5 DAC. We have done this enabling 200 pixels in the Cascode FE

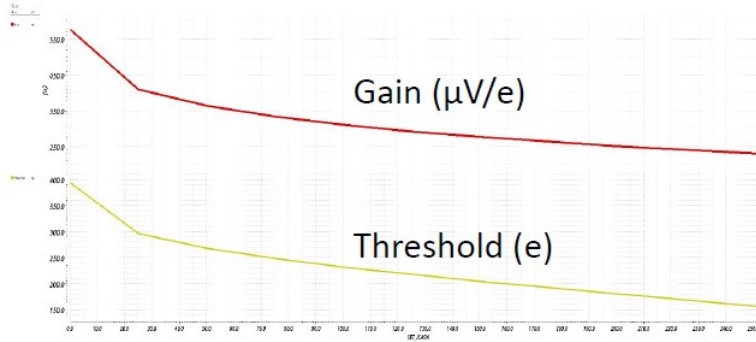


Figure 2.25: Trends of Gain and Threshold increasing I_{CASN} .

(rows: 472 - 512, cols: 225 - 230).[??]

The threshold distributions have been fitted with a gaussian function for each measurement, in order to obtain the average values and their dispersion.

In figure 2.26 all trends obtained from these data are reported.
[TREND OF DISPERSION?]

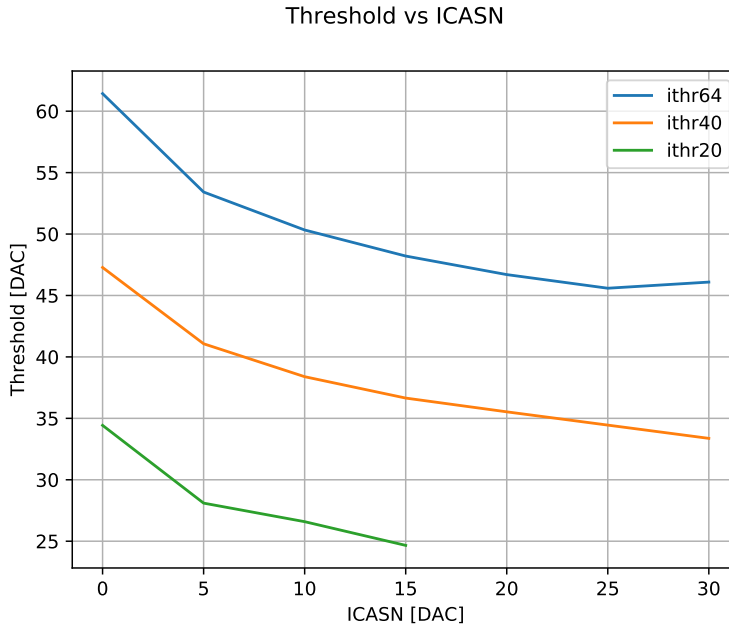


Figure 2.26: Threshold vs. I_{CASN} for $I_{THR}=20, 40, 64$.

2.5.2.2 I_{THR}

Reusing the same data of the previous measurements, the trend of the threshold have been studied, changing the value of I_{THR} and fixing that of I_{CASN} . In this

case only I_{CASN} from 0 to 15 DAC is considered, because for higher values we don't have enough measures of the threshold (specifically only two for $I_{THR}=40, 64$). The results are shown in figure 2.27.

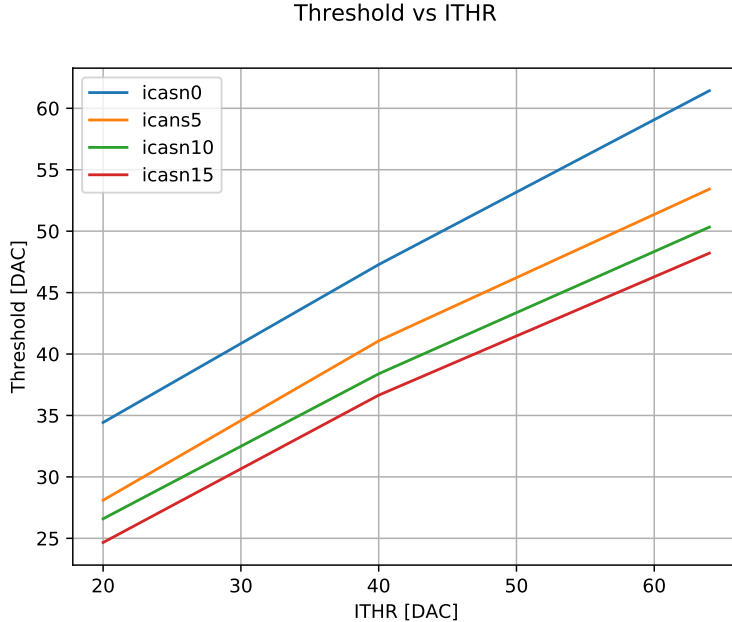


Figure 2.27: Threshold vs. I_{THR} for $I_{CASN} = 0, 5, 10, 15$.

We can compare them with the simulation done by Hung Pham in figure 2.28 on the facing page.

2.5.2.3 Time over Threshold (ToT)

The last analysis done in order to make a comparison with the simulations, is about the trend of the ToT changing the value of I_{CASN} for a fixed value of I_{THR} and vice versa. In particular we consider the data obtained with I_{CASN} fixed to 0 DAC and I_{THR} to 64 DAC, which are the values studied and used for this registers during the Test Beam in Desy.

2.5.2.4 some nice picture of the optimized thr and tuning

!!!!!!!!!!!!!!

2.6 Cross talk issue and mitigation

As it was already pointed out, during the measurements of the average threshold of all FE (section REFERENCE), there were something atypical in the s-curves of the HVs flavor, because some of pixels seem to have occupancy greater than 1. This behavior threatens the good functionality of the overall matrix response,

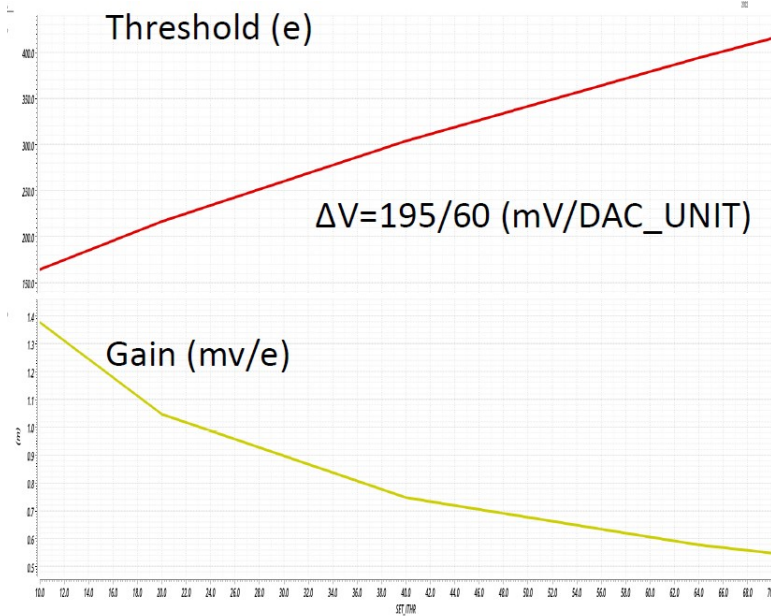


Figure 2.28: Trends of Gain and Threshold increasing I_{CASN} .

because some pixels flood the readout, giving floating results.(all readout process)

Also during the systematic study of the main registers' values, the presence of the hot pixels has prevented to use certain settings and as consequence to reach lower global thresholds.

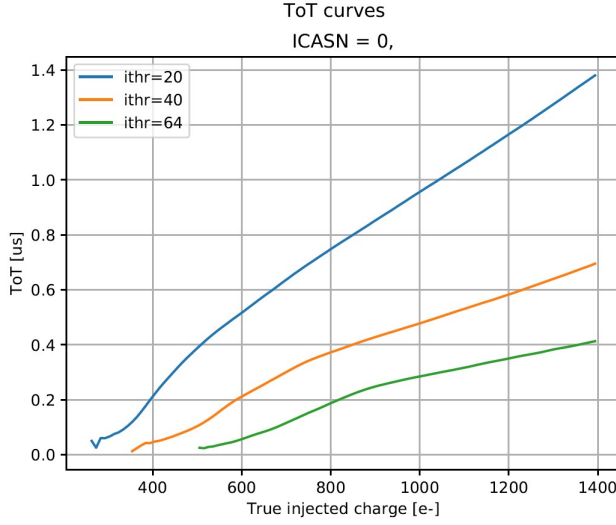
For this reason an investigation has been conducted in order to understand the reasons why and to cure them as far as possible. During this study an important issue with cross-talk(readout signal) was discovered, and so in this section we examine this effect and some attempts(tries) to mitigate it using different settings/bias.

2.6.1 Hot pixel issue

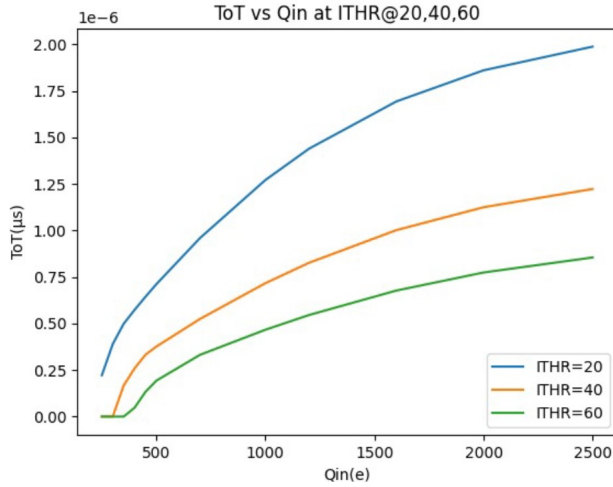
First of all we noticed that in the s-curves oh the HVs flavor, for example that of HV-Cascode in figure on page ??, the atypical behavior could be triggered by a digital signal sent to the matrix during the readout activity at low threshold, for two main reasons:

- when the matrix has high threshold, like for Normal and Cascode FE, all pixels seem to behave as expected.

Lowering the threshold and running some source acquisitions without any source no strange behaviour was observed. Acquiring data with a radioactive source instead, even Normal and Cascode FE seem to reveal the same problem. This led to thinking that during the readout of good pixels an induced signal is created which couples with some other pixels, in particular with those at lower threshold with respect to the average value. If



(a) ToT vs I_{THR} ($I_{CASN}=0$ DAC) - Data (Cascode)

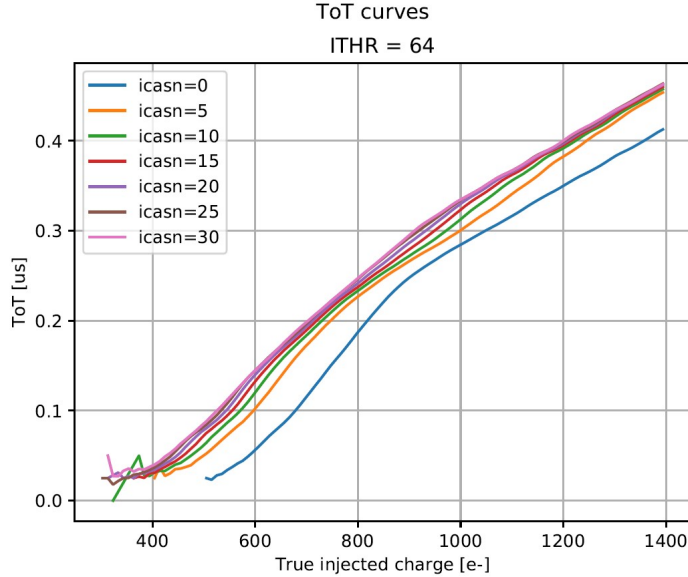


(b) ToT vs I_{THR} ($I_{CASN}=0$ DAC) - Simulation

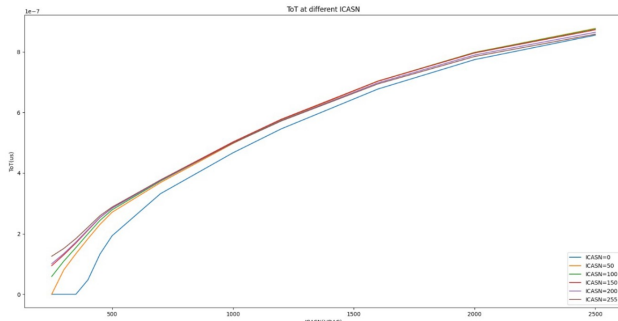
Figure 2.29: ToT vs I_{THR}

the height of this signal exceed the threshold of the single pixel, it causes some spurious hits, making the pixel "**hot**".

- Moreover, considering the HV Cascode s-curves, it could be noticed that in the region before the threshold ($(Q_{inj} < \text{threshold})$, pointed by the blue arrow) there isn't an anomalous activity which means that the induced signal is not due to the BCID that is always sent to the matrix during the injection or an acquisition with the source, regardless of being above or below the threshold. The atypical behaviour indeed, is in the region above the threshold ($(Q_{inj} > \text{threshold})$, pointed by the red arrow) where the occupancy of some pixels becomes greater than 1. This means that these



(a) ToT vs I_{CASN} ($I_{THR}=64$ DAC) - Data (**Cascode**)



(b) ToT vs I_{CASN} ($I_{THR}=64$ DAC) - Simulation

Figure 2.30: ToT vs I_{CASN}

hot pixels detect more hits of those injected.

From these first observations, we have reached the conclusion that the cross talk could be tied to the readout activity. So we have started investigating the timestamp of the hits (out of synch) not synchronize with the timestamp of the injection.

2.6.2 Hot pixel strategy (study)

At first, it has been lowered the threshold in order to "create" hot pixel also in the first two flavors of the matrix. In fact with TB settings the threshold was too high and the hypothetical induced signal didn't caused spurious hits. For this purpose (to this end, to do this) different settings were tried, changing some fundamental registers responsible for the threshold like those listed and explained on page 37.

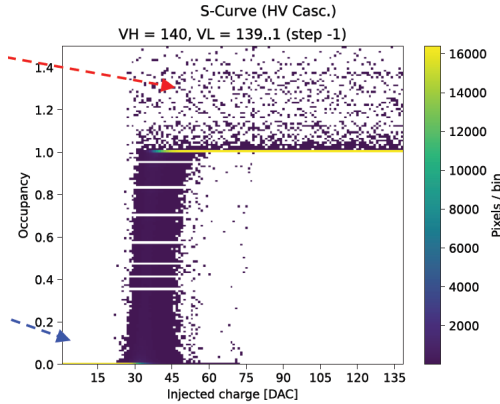


Figure 2.31: HV-Cascode s-curves.

Then it was tried to run tests under controlled conditions:

- one healthy(good) pixel was injected;
- one *hot pixel* (or two or three in next test) was enabled but not injected;
- the all matrix except these pixels was disabled.

In this way (thus) (remembering the readout sequence [REFERENCE]) the readout cycle had a known duration and two timing info and some precautions had been used to study the induced signal with greater precision:

- ΔTS (TimeStamp) between two consecutive hits: the TimeStamp is assigned from the FPGA when the TOKEN rises on the TE of the first hit to read, but only if the previous readout frame is completed. So, if the hit coming from a *hot pixel* is after the hit from the injected one, the minimum ΔTS has to be equal to the readout time of 1 pixel and so the duration (period) of the signal FREEZE_STOP.
This info has allowed to verify if the hot pixel fires after the good injected one or not.
- LE(hit) - TE(previous hit): this quantity measures the elapsed time between a hit and the previous one. This is a finer info than the ΔTS because it allows to correlate the hit with the induced digital signal, originate from the readout cycle.

Moreover, since a 7-bit BCID is sent to the matrix during its activity, it was important to keep short (<128 clock cycle) the duration of the full readout sequence and to not enable too many pixels in order to not extend too much the readout frame. Otherwise the information on the leading edge of the pixel could not be correlated with the token of the previous hit. In other words, if the readout frame exceed 128 clock cycles, since the token could be raised if the matrix is **not** freeze, even if an hit is arrived before it could be read only in the next frame when it could rise again the token, but in this case it will have different TimeStamp. So in this case the TS is useless for our purpose.

2.6.3 Cross-talk (Results)

Referring to the readout sequence explained in section [REFERENCE], in order to understand which signal could induce cross talk, each register's value has been moved one by one. In table on the current page just an example of the several settings tried.

Register	Value
FREEZE_START_CONF	10
READ_START_CONF	13
READ_STOP_CONF	15
LOAD_CONF	30
FREEZE_STOP_CONF	31
STOP_CONF	31

Table 2.6: Registers of the Readout cycle.

Doing so indeed, the LE-TE info has to shift by the same value, in correspondence with the signal that cause the cross talk. This step of the procedure is tied with the necessity to keep the readout sequence within the maximum 128 BCID range.

For example, if FREEZE_START_CONF is responsible for the cross talk signal, shifting its value by a certain amount, we expect that the hot pixels start to fire after that this signal arises due to the hit on the injected pixel. So the value of LE-TE has to be FREEZE_START_CONF + some potential(possible, probable) delay. Same argument for the other registers.

By this procedure, repeated for each readout register, we have come to the conclusion that the cross-talk could be related to the raising and falling edge of the FREEZE signal.

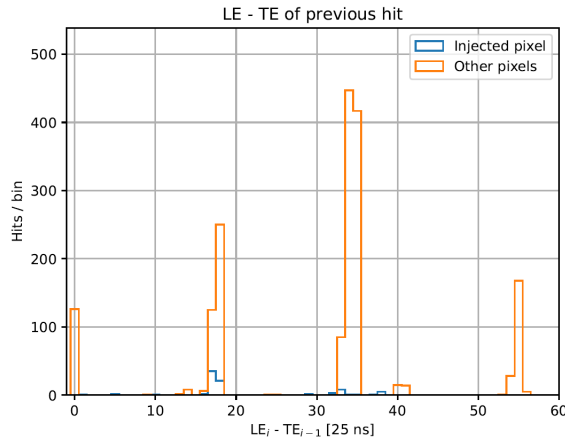
In figure on the following page an example of some results obtained. It is the histogram of the time last between the leading edge of an hit and the trailing edge of the previous hit, when one pixel is injected and two are read. It's possible to see several peaks (referring to the readout setting reported in table on the current page):

- one at 0, that represent the situation in which both hits come from hot pixel firing simultaneously after the injection. This means that they are activated by the same signal and so is the most important confirmation that is cross-talk and not random firing pixel signal;
- one at ≈ 18 equal to FREEZE STAR raising + 8 \rightarrow first induced signal;
- one at ≈ 35 equal to FREEZE STOP falling + 4 \rightarrow second induced signal;
- one at ≈ 55 equal to FREEZE STOP falling + 4 when two different pixels are read (specifically in this case after the first 30 time unit until the LOAD CONF, a distinct pixel reading starts and it last another 20 time unit (LOAD - FREEZE START) + 1 unit time to conclude the

frame with the FREEZE STOP and so $51 + 4$ unit time wrote above. So when two pixels are read, the FREEZE STOP falling after 51 clock cycles, and it is compatible with the last peak in the plot.

Injected pixel: (217, 140)							
Other pixels: [(218, 155) (222, 188)]							
Assuming timestamp clock = 40.00 MHz							
Green = injected pixels							
Row	Col	LE	TE	ΔLE	ΔTE	ΔTS[25ns]	TS[25ns]
140	217	12	29	124	123	5627.0000	635972.0000
140	217	8	25	124	124	5628.0000	641600.0000
155	218	60	60	52	35	35.0000	641635.0000
188	222	59	60	127	0	0.0000	641635.0000
155	218	115	115	56	55	55.0000	641690.0000
188	222	114	115	127	0	0.0000	641690.0000
155	218	42	43	56	56	55.0000	641745.0000
188	222	42	42	0	127	0.0000	641745.0000
140	217	4	21	90	107	5482.0000	647227.0000

(a) An example of the time quantity used in the analysis.



(b) An example of the LE(hit)-TE(previous hit) histogram.

Figure 2.32: Some results of the cross-talk studies.

As already stated, we run several tests varying the number of pixels to read, the value of the readout registers, different combination of hot and good pixels and also different spatial location of them in the matrix to exclude the possibility that the problem was related to particular columns. All results are in agreement with the interpretation explained above.

MAH...

Furthermore it has been tried to estimate the height of the induced signal from the threshold of the hot pixel. For this reason we have tried different setting of the currents cited above to make a pixel *hot* in order to understand when the induced signal went above the threshold. We have found that the signal could (may) correspond to 100/150 e^- .

In figure on the facing page an analog acquisition of the readout signals taken

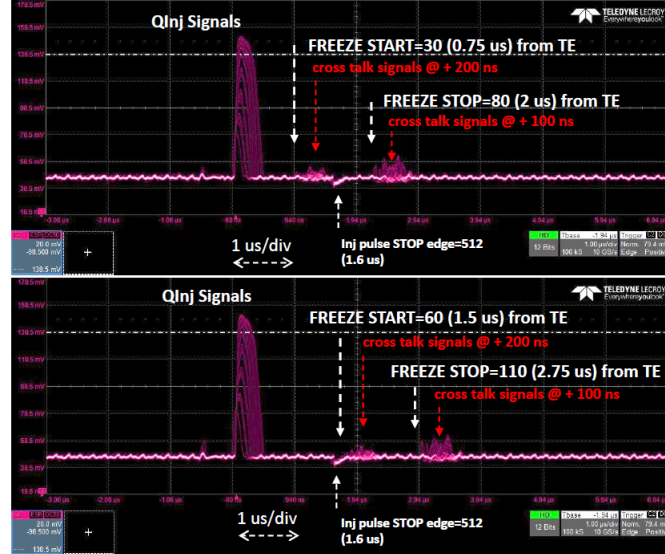


Figure 2.33: Cross-talk of the FREEZE signal on oscilloscope's analog output, for different value of FREEZE_START_CONF register.

by an oscilloscope.

In these tests one pixel was injected from 0 to 140 DAC (in the acquisition it can be seen in the increasing signal height). There are two different group of spikes, the first which smaller and represent the cross-talk from the raising of the FREEZE signal and the second, larger and corresponding to the cross talk from the falling edge of the same signal. Moreover it's possible to see that in the two different pictures, the cross talk signals move according to the different settings of the FREEZE START/STOP edge.

2.6.4 Mitigation

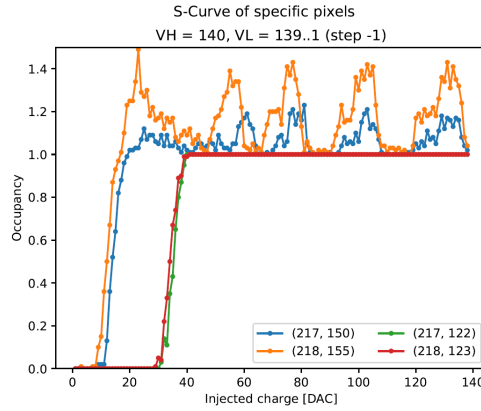
As seen in the previous, the problem of the hot pixel is tied to the induction signal produced during the readout which cause cross-talk. It becomes more important(significant, serious) when there is grater dispersion threshold.

Potentially every pixel could become *hot* if its threshold is lower than the height of the cross-talk signal since the FREEZE is sent across the entire matrix.

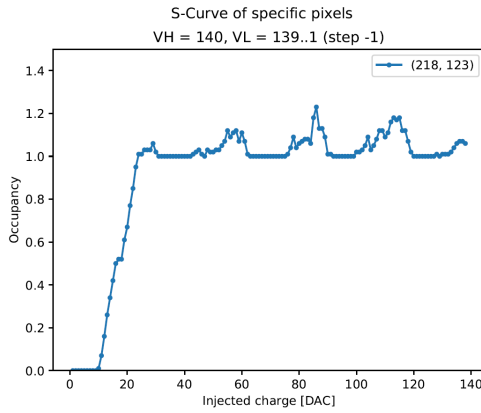
As an example in figure on page ?? it si possible to compare the behaviour of pixel (218, 123) changing(modifying) some registers' values in order to reduce the threshold.

For this reason, a possible treatment could be related to the threshold tuning, explained in section (reference) , which could allow to make the pixels threshold more uniform (less threshold dispersion) and simultanously targeting a value greater than the induced signals.

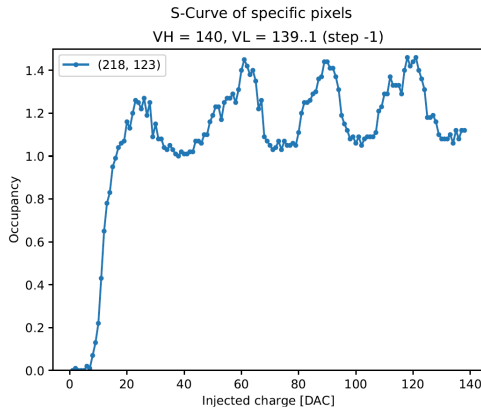
In figure on page 49 an example of the results obtained.



(a) $I_{DB}=100, I_{TUNE}=53$ - Good behavior



(b) $I_{DB}=60, I_{TUNE}=150$ - Pixel starts to misbehave



(c) $I_{DB}=55, I_{TUNE}=150$ - Pixel becomes *hot*

Figure 2.34: S-curve of the pixel (218, 123) for different register settings.

It's evident the reduction of the tail in the threshold distribution, in fact the

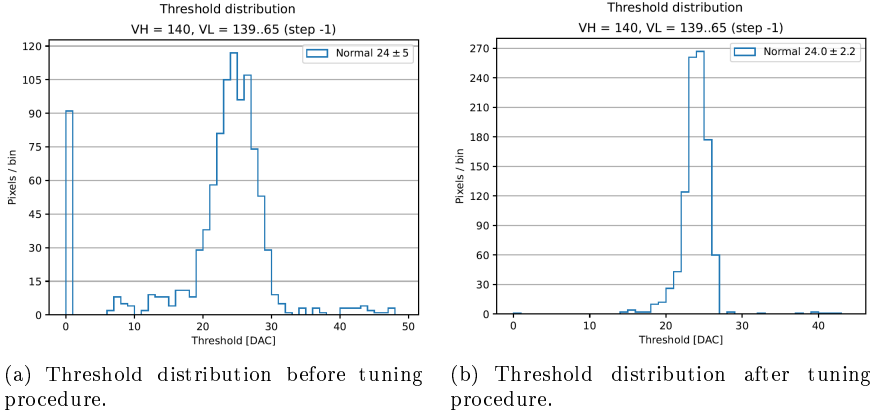
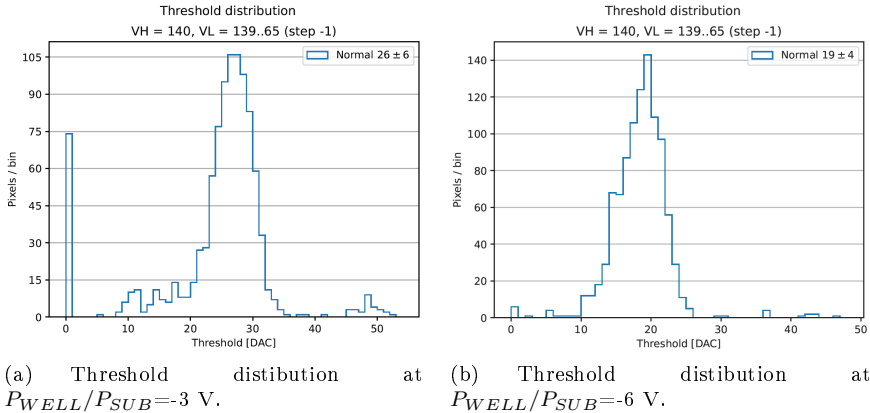


Figure 2.35: Threshold tuning to reduce hot pixels.

dispersion is reduced by 56%. Also the hot pixels decrease from 18% to 1.2% of the total number of pixels studied. [We can noticed indeed that the peak at 0 threshold disappears.]

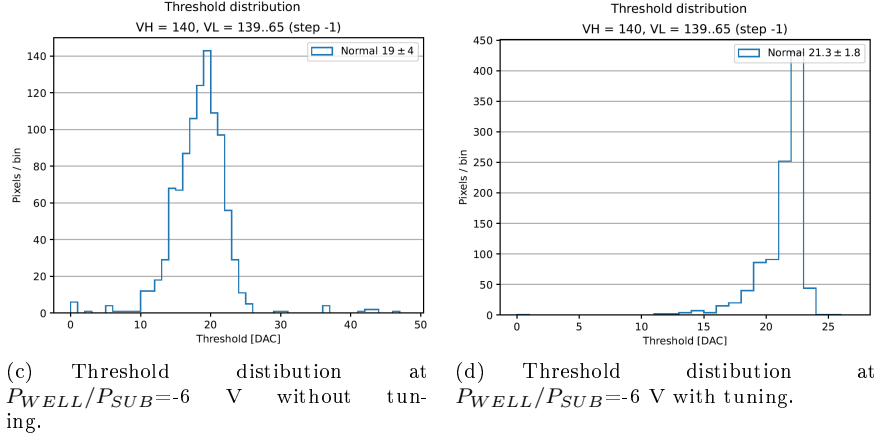
Moreover it has been tried to increase the voltage bias of the all matrix, too. We remember that all previous test has been run with P_{WELL}/P_{SUB} set to -3 V. This value was increased to -6 V and indeed there were some improvements. In fact increasing the bias, we expected a decrease of the diode capacitance thus higher gain and lower thresold dispersion. In addition the coupling with the cross talk signal is reduced too and so the induced signal height. In figure on the current page a comparison between the threshold distribution respectively at -3 V and -6 V, with same registers setting and without tuning.



At higher bias voltage not only is the threshold lower (higher gain), but also its dispersion, as expected. And despite that there are fewer hot pixels: 1.3% at -6V against 17% at -3 V. Also here it's clear a reduction of the threshold distribution tail.

2.6.4.1 Final results?

Eventually the final results obtained with both threshold tuning and a bias voltage on $P_{WELL}/P_{SUB} = -6$ V.



As we can see in figure on this page, the threshold dispersion decreases with the number of hot pixels. In fact without tuning there are 1.3% of them, instead with tuning procedure there are none at all.

2.7 Test Beam results

Hit detection efficiency from bespin article

3. Conclusions

List of Figures

1.1	Particle classification in the Standard Model.	5
1.2	SuperKEKB accelerator in 2021. The letters V and H denote respectively vertical and horizontal collimators. Each ring is divided in 12 sections, from the first called D01 to the last D12.	9
1.3	Beam energies to reach center of mass energy equal to $\Upsilon(4S)$, $\Upsilon(6S)$, 11.24 GeV and 12 GeV. Horizontal axis represents the energy of LER and the vertical one the energy of HER.	10
1.4	Comparison between the beams scheme used in KEKB and SuperKEKB.	11
1.5	Belle II detector.	11
1.6	A schematic view of the Belle II vertex detector with a Be beam pipe and the six layers of PXD and SVD.	12
1.7	TOP detector.	13
1.8	ARICH detector.	13
2.1	The W14R12 chip tested during the Test Beam in Desy.	16
2.2	Detection efficiency map of a TJ-Monopix1 chip with 25 μm p-epitaxial layer that has been irradiated to $10^{15} n_{eq}/\text{cm}^2$ NIEL.	16
2.3	The layout of the TJ-Monopix2 prototype divided in four different flavors: Normal , Cascode , HV-Cascode and HV FE	17
2.4	Layout of a TJ-Monopix 2 2x2 pixel core. In blue the analog area and in yellow the digital one.	18
2.5	An example of the S-Curve fitted by the CDF to evaluate threshold and noise.	20
2.6	S-curves of all pixels of the Normal FE with an injection pulse of 140 DAC.	21
2.7	Normal FE.	22
2.8	S-curves of all pixels in the Cascode flavor with an injection pulse of 140 DAC.	22
2.9	Cascode FE.	23
2.10	S-curves of all pixels in HV Cascode flavor with an injection pulse of 140 DAC.	24
2.11	HV Cascode FE.	24
2.12	S-curves of all pixels in HV Cascode FE with an injection pulse of 140 DAC.	25
2.13	HV Normal FE.	25
2.14	HV's FE.	25
2.15	Schematic of 3-bit tuning DAC (TDAC)	27

2.16	ToT curves fit for all frontend.	29
2.17	^{55}Fe peaks for all frontends.	31
2.18	^{241}Am γ emission spectrum.	31
2.19	^{241}Am peaks for all frontends.	32
2.20	^{109}Cd pekas for all frontends.	33
2.21	Injection capacitance distributions of all FE.	34
2.22	ToT linearity of all flavors assuming the nominal(expected) conversion factor equal to $10.1 \frac{e^-}{DAC}$.	36
2.23	ToT linearity of all flavors assuming the conversion factor obtained from calibration for each FE.	37
2.24	Summary of trends.	38
2.25	Trends of Gain and Threshold increasing I_{CASN} .	39
2.26	Threshold vs. I_{CASN} for $I_{THR} = 20, 40, 64$.	39
2.27	Threshold vs. I_{THR} for $I_{CASN} = 0, 5, 10, 15$.	40
2.28	Trends of Gain and Threshold increasing I_{CASN} .	41
2.29	ToT vs I_{THR} .	42
2.30	ToT vs I_{CASN} .	43
2.31	HV-Cascode s-curves.	44
2.32	Some results of the cross-talk studies.	46
2.33	Cross-talk of the FREEZE signal on oscilloscope's analog output, for different value of FREEZE_START_CONF register.	47
2.34	S-curve of the pixel (218, 123) for different register settings.	48
2.35	Threshold tuning to reduce hot pixels.	49

List of Tables

2.1	Settings of the main registers used for all flavors (W14R12 chip) during the Test Beam in Desy.	21
2.2	Summary table of threshold and noise values for all flavors of the W14R12 chip.	26
2.3	Threshold and parameters obtained from the fit of ToT curve for each frontend.	28
2.4	Emission lines of ^{55}Fe , ^{241}Am , ^{109}Cd sources visible by the sensor.	30
2.5	Estimation of injection capacitance of all flavors for different source emission peaks.	35
2.6	Registers of the Readout cycle.	45